

Condensation dynamics of sticky and anchored flexible biopolymers

Adam R. Lamson^{*1,2}, Mohammadhossein Firouznia¹, and Michael J. Shelley^{1,3}

¹Center for Computational Biology, Flatiron Institute, New York, NY 10010 USA

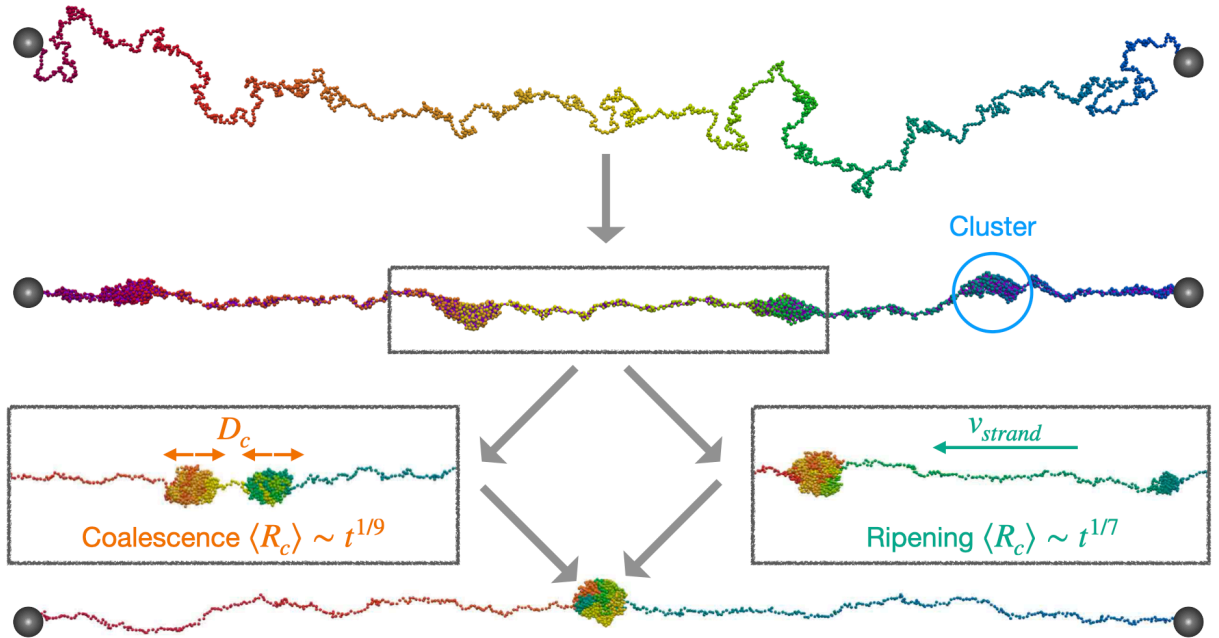
²Cluster of Excellence Physics of Life, TU Dresden, Dresden, 01307 Germany

³Courant Institute, New York University, New York, NY, 10012 USA

*Email: alamson@flatironinstitute.org

Abstract

Cells regulate gene expression in part by forming DNA–protein condensates in the nucleus. While existing theories describe the equilibrium size and stability of such condensates, their dynamics remain less understood. Here, we use coarse-grained 3D Brownian-dynamics simulations to study how long, end-anchored biopolymers condense over time due to transient crosslinking. By tracking how clusters nucleate, merge, and disappear, we identify two dominant dynamical pathways, ripening and merging, that govern the progression from an uncompacted chain to a single condensate. We show how microscopic kinetic parameters, protein density, and mechanical constraints shape these pathways. Using insights from the simulations, we construct a minimal mechanistic free-energy model that captures the observed scaling behavior. Together, these results clarify the dynamical determinants of DNA and chromatin reorganization on timescales relevant to gene regulation.



Introduction

Biopolymers provide the structural and functional framework for many biological processes. From RNA and amino acid chains to cytoskeletal filaments and chromatin, organisms rely on the precise organization of these macromolecules to sustain cellular functions [1]. Among them, chromatin—the complex of DNA and histone proteins within eukaryotic nuclei—is particularly remarkable. A single human chromosome, comprising approximately 10^8 nucleotides ($\sim 10^4 \mu\text{m}$), is intricately compacted into a nucleus of $\sim 10 \mu\text{m}$ in diameter [68]. Recent studies have revealed that chromatin is not merely a passive carrier of genetic information but a highly organized, dynamic structure [33, 45, 2]. Disruptions to chromatin organization have been linked to developmental disorders, cancer, and other diseases [76, 19, 31, 17, 34].

This organization is maintained by a diverse set of proteins that selectively bind, interpret, and remodel chromatin, dynamically shaping genome accessibility and activity [4, 24, 13, 26]. A central question in nuclear organization is how cells establish and regulate a chromatin state that is both highly structured and adaptable. One proposed strategy is biomolecular condensation, where proteins transiently associate with chromatin by binding to DNA, histones, and other nuclear factors, driving self-association and therefore compartmentalizing or clustering of genomic regions [55, 57]. This process plays a fundamental role in genome function, influencing transcriptional regulation, DNA repair, and the establishment of epigenetic modifications [23, 47, 11].

The dynamic reorganization of chromatin takes place within the complex and crowded nuclear environ-

ment, where chromatin is tethered to nuclear structures such as the lamin fibers lining the nuclear envelope and the nucleoli [75, 2, 50]. This raises the fundamental question of how passive nuclear proteins, such as HP1, orchestrate the large-scale reorganization of chromatin within confined and geometrically constrained nuclear environments while ensuring the speed and selectivity required for proper cellular function.

In vivo studies of nuclear hubs, speckles, and other condensates have demonstrated chromatin organization's importance in cellular function. Single-molecule *in vitro* experiments complement such experiments by elucidating the polymeric and physical principles governing DNA-protein condensation [20, 29, 52, 43, 53, 62]. By manipulating DNA and chromatin segments between optically trapped beads, experiments measure forces, molecular interactions, and protein distributions along the polymers [71, 35, 52, 46]. Furthermore, assays have also recreated the dynamic organization of DNA using *Xenopus* egg extract containing all the proteins present in nuclear environments [66].

Such research has revealed that protein-protein interactions within nuclear condensates are often mediated by the intrinsically disordered regions (IDRs) of DNA-binding proteins [42]. These interactions, typically on the order of $1 k_B T - 3 k_B T$ [43, 58], are individually weak but collectively generate sufficient force to drive chromatin condensation [52, 53, 62, 74]. Additionally, specific proteins exhibit prewetting behavior, coating DNA in a monolayer and, at higher protein concentrations, form droplets or condensed homogenous polymer-protein mixtures known as co-condensates [43, 53]. Phenomenological equilibrium models, which account for polymer entropy, surface tension, and droplet free energy, provide a framework for predicting phase transitions. However, they do not explain how clusters of proteins and nucleic acids dynamically reorganize to reach equilibrium. Addressing this question is essential for linking *in vitro* observations to the complex, non-equilibrium behavior of chromatin in living cells.

Pioneering work by De Gennes [12] and others [32, 21] explained how strong attractive interactions between segments of a freely draining chain collapses the polymer in a multi-step process. Later confirmed by simulations, this process begins as an initially extended polymer reconfigures into a two-phase structure consisting of dense clusters connected by stretched segments. In this long-lived 'pearl-necklace' phase, the polymer ends are gradually drawn together as the system relaxes, decreasing the number of clusters over time and increasing the fraction of polymer in the dense phase [21]. The reduction in cluster number is governed by two competing mechanisms: direct coalescence of spatially adjacent clusters and a 'curious' Ostwald ripening process, wherein polymer is pulled from one cluster into another [32]. The relative contributions of these mechanisms and the microscopic determinants that drive polymer reorganization remain open questions, especially in biological contexts.

When a polymer is constrained at both ends— as sections of chromatin may be when tethered to the nuclear periphery by lamin fibers or DNA manipulated in optical trap experiments—the reduction in cluster

number slows, and the total amount of polymer in the clustered phase becomes limited [9, 21, 39]. Previous studies on constrained polymer systems found that dense clusters diffuse along the polymer backbone, facilitating the relaxation towards a monolithic cluster [3, 61, 67, 7]. However, these studies often overlooked biologically relevant attributes of DNA-binding proteins, such as limited binding valency between proteins or the collective viscoelastic properties that emerge from protein-protein and protein-polymer association. [64, 8, 42, 65, 44]. Moreover, the time integration methods used in early computational studies are known to overestimate diffusive behavior, leading to conclusions that neglect the ripening mechanisms mentioned above. While later studies have addressed some of these limitations, they have not directly reported on the basic determinants and dynamics of homopolymer relaxation [30, 47, 27, 69]. In order to accurately model biofilaments, it is essential to incorporate physical principles intrinsic to DNA binding proteins and their interactions.

To model large numbers (hundreds to tens of thousands) of mesoscale biological structures (e.g., nucleosomes, IDRs, HP1 α) in a computationally tractable way, we turn to coarse-graining methods. One approach to capturing transient interactions is the sticker-spacer model, which simplifies amino acids in IDRs into different species of interacting spheres, greatly improving computational efficiency compared to atomic-level molecular dynamic simulations. However, the size disparity between histones and amino acids remains a challenge, preventing these simulations [41, 38] from reaching biologically relevant timescales (minutes to hours). To overcome this limitation, we couple coarse-grained polymer dynamics with a kinetic Monte Carlo scheme that models protein-mediated crosslinks as transient harmonic springs between DNA segments. Binding and unbinding events obey detailed balance, ensuring that protein association does not artificially alter polymer relaxation dynamics [30, 36]. We employ a novel semi-implicit collision resolution algorithm to accurately resolve excluded volume interactions between polymer segments. This prevents unphysical behavior such as complete system collapse while still allowing the system to reach equilibrium [72]. Unlike conventional hard-core potential methods, our approach avoids numerical stiffness and remains computationally efficient and accurate.

Using our simulations, we demonstrate how the interplay between polymer diffusion, protein-mediated crosslinking, and spatial constraints governs the macroscopic condensation dynamics. We identify the collapse pathways of flexible biopolymer driven by transiently crosslinking proteins in both *in vitro* and *in vivo* systems. Building on these insights, we develop a minimal model that predicts and explains the long-time behavior of collapsing polymers. Combined with numerical simulations, this model unifies previous theoretical frameworks for synthetic constrained polymers and the reorganization of biopolymers under confined conditions. One key advance is the ability to directly link the microscopic properties of DNA-binding proteins to the macroscopic and phenomenological parameters commonly used in DNA dynamics

Brownian Dynamics Model (*aLENS*)

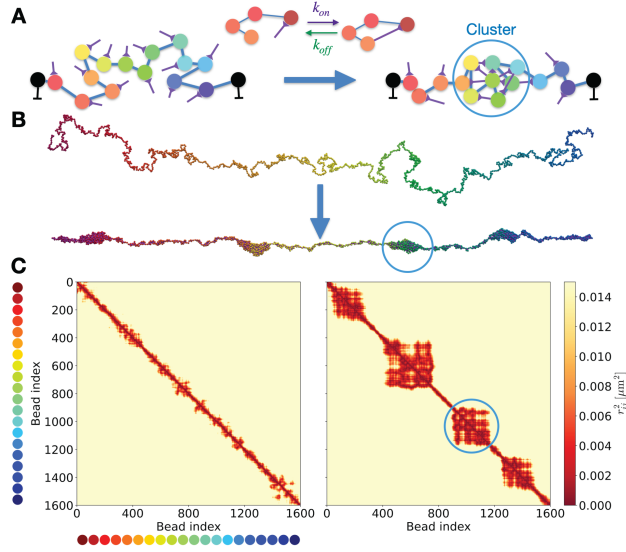


Figure 1: (A) Schematic representation of a polymer chain with sticky tails and fixed ends. The color of the beads indicates their index, with black representing the two fixed ends. Sticky tails are depicted as purple bars attached to the beads. Under the influence of kinetic binding (indicated by purple and green arrows), sections of the chain form dense clusters (light blue circle). (B) Simulation snapshots at $t = 0$ s (top) and after undergoing condensation at $t = 600$ s (bottom). An example cluster is circled in light blue. (C) Bead distance maps from the snapshots shown in (B). The left (right) plot is calculated from bead positions at $t = 0$ s ($t = 600$ s). The circled cluster in (B) corresponds to the region marked in light blue in the right plot.

To model constrained polymer collapse driven by crosslinking proteins, we consider a self-interacting, freely draining bead-spring chain. For a chain consisting of N beads, the system configuration is represented by the vector

$$\mathcal{C} = [\mathbf{R}_1, \dots, \mathbf{R}_N]^T \in \mathbb{R}^{3N}, \quad (1)$$

where \mathbf{R}_i is the 3D position vector of the i -th bead. The system's motion is governed by the overdamped Langevin equation:

$$\dot{\mathcal{C}} = \mathbf{u} = \mathcal{M} (\mathcal{F}_B + \mathcal{F}_C + \mathcal{F}_X) + \mathbf{u}_n, \quad (2)$$

where \mathbf{u} is the the grand velocity vector, $\mathcal{M} \in \mathbb{R}^{3N \times 3N}$ is the mobility matrix, and $\mathcal{F}_{B,C,X} \in \mathbb{R}^{3N}$ are forces arising from harmonic springs connecting beads in the polymer chain, collision forces, and forces due to crosslinking, respectively. The term \mathbf{u}_n accounts for thermal fluctuations and satisfies the fluctuation-

dissipation theorem by being drawn from a Gaussian distribution such that

$$\langle \mathbf{u}_n \rangle = \mathbf{0} \quad \langle \mathbf{u}_n(t) \mathbf{u}_n(t')^T \rangle = 2 k_b T \mathcal{M} \delta(t - t'), \quad (3)$$

with the Boltzmann constant k_b and temperature T . Hydrodynamic interactions between beads are neglected. As a result, the mobility matrix for a freely draining chain with spherical beads is diagonal, with elements given by the Stokes-Einstein relation $\mathcal{M} = (3\pi\eta b)^{-1} \mathbf{I}^{3N}$, where \mathbf{I}^{3N} is the $3N \times 3N$ identity matrix, η is the viscosity of surrounding fluid, and b the diameter of the beads. To replicate the experimental conditions involving constrained or tethered chains, the first and last beads of the chain are fixed in space (Fig. 1). For these fixed beads, the associated mobilities and noise terms are set to zero.

The positions of beads are integrated through a linearized Euler time-stepping scheme [72]

$$\mathbf{c}^{k+1} = \mathbf{c}^k + \mathbf{u}^k \Delta t \quad (4)$$

However, forces arising from harmonic bonds and those due to hard collision potentials introduce numerical stiffness to the problem, restricting the timestep size when treated explicitly. Therefore, we calculate the bead velocities \mathbf{u}^{k*} by solving a constraint optimization problem. This approach improves numerical stability and allows us to achieve biologically relevant timescales in simulations. We enforce hard steric interactions, which prevents bead overlaps and permits chain entanglement, through a complementarity constraint. For bead pairs i, j , separated by distance $r_{ij} = |R_i - R_j|$ we ensure that the inequalities

$$\begin{aligned} \text{No contact: } r_{ij} - b &\geq 0, & f_{C,ij} &= 0, \\ \text{Contact: } r_{ij} - b &= 0, & f_{C,ij} &\geq 0, \end{aligned} \quad (5)$$

are satisfied at every timestep by solving for \mathbf{u} . $\mathbf{f}_C \in \mathbb{R}^M$ is the vector of constraint force magnitudes with dimensionality M equal to the number of pairs within a search radius set for computational efficiency. The directed constraint forces are calculated by constructing a sparse directed matrix $\mathcal{D}(\mathbf{C}) \in \mathbb{R}^{3N \times M}$ such that $\mathcal{F}_C = \mathcal{D} \mathbf{f}_C$.

All bonds are taken to be harmonic with a given rest length resulting in a force magnitude matrix

$$\mathbf{f}_B = -\mathcal{K}_B(\mathbf{r}_B - b\mathbf{1}^{N-1}) \quad \text{and} \quad \mathbf{f}_X = -\mathcal{K}_X(t)(\mathbf{r}_X - l_X\mathbf{1}^{N_X}), \quad (6)$$

where the polymer stiffness matrix \mathcal{K}_B and crosslinking matrix \mathcal{K}_X are diagonal with entries equal to the spring constants κ_{DNA} and κ_X , respectively (Table 1). Here $\mathbf{1}^N = [1, \dots, 1]^T \in \mathbb{R}^N$, and $\mathbf{r}_B =$

$[r_{01}, \dots, r_{ii+1}, \dots, r_{N-2N-1}]^T \in \mathbb{R}^{N-1}$ and $\mathbf{r}_X \in \mathbb{R}^{N_x}$ contain the distances between pairs of permanently and transiently bonded beads, respectively. To form a polymer chain, \mathbf{r}_B is defined so beads are connected to neighbors in index space with rest lengths equal to the bead diameter. Crosslinking bonds have a fixed rest length ℓ_X . The transient nature of the crosslinking bonds means that the size of \mathcal{K}_X changes, $N_X = N_X(t)$. The direction of these forces is assigned similarly to collision forces. At each timestep, the forces \mathbf{f}_C , \mathbf{f}_B , and \mathbf{f}_X are computed by formulating the discretized equations of motion as a quadratic programming problem [73, 72]. Both spring and collision forces are resolved at every timestep using a fast global optimization algorithm.

The polymer chains are subject to transient crosslinking or *sticky tails*. These sticky tails model biologically reactive components such as intrinsically disordered regions (IDRs) of DNA/chromatin binding proteins, linker histone H1, or histone tails [49, 18, 48, 41, 53, 52]. These tails are simplified to allow simulation of systems with $10^3 - 10^4$ beads over timescales ranging from minutes to hours. The tails can be viewed as harmonic springs with one end permanently bound to a base bead (the *base end*) and the other end capable of binding and unbinding to neighboring beads (the *transient end*). When only the base end is bound, the tail exerts no force on the polymer. However, the tail's transient end binds to other beads probabilistically according to an Arrhenius-like law:

$$k_{on}(r_{ij}) = k_o \exp\left(-\frac{\Delta G(r_{ij})}{k_B T}\right), \quad (7)$$

where k_o sets the timescale of the reaction. This treatment implicitly satisfies detailed balance if the transient end unbinds at the rate $k_{off} = k_o$ and the difference in free energy takes the form

$$\Delta G(r_{ij}) = \epsilon_1 + \frac{\kappa_x}{2} (r_{ij} - l_X)^2. \quad (8)$$

The first term, ϵ_1 , in equation (8) accounts for the binding energy and is associated with the binding equilibrium constant K_e by $\epsilon_1 = \ln\left(\frac{k_{on}(0)}{k_{off}}\right) = \ln(K_e)$. The second term is the enthalpic contribution from the spring's potential energy. For simplicity, force-dependent unbinding is not considered in this model. Although there is no explicit limit on the number of transient ends that can attach to a bead, steric interactions limit the local density of neighboring beads. Given the exponentially decaying form of the binding rate in equation (7), the effective maximum number of attachments is set by the tails' spring constant, rest length, temperature, bead diameter, and number of tails per bead n_x . According to this model, for weak springs or long rest lengths, the tails may bind through beads in dense clusters. To avoid unphysical behavior, we have selected values for tail lengths and spring constants that are consistent with

biological structures (Appendix).

Results

Here, we investigate a constrained polymer chain whose condensation is induced by transient crosslinking proteins. The self-organization driven by transient bonds accounts for the attractive interactions typical of intrinsically disordered regions (IDRs) found in transcription factors and other DNA-binding proteins [49, 70, 41, 6, 53, 52]. The chains' fixed ends simulate scenarios such as optical trap experiments or nuclear environments, where condensing DNA regions are restricted by tethering or frictional forces.

Experimental evidence suggests that both mechanical constraints and kinetic interactions are important for protein-mediated biopolymer organization [16, 14, 5, 29]. We examine, in particular, how the association constant K_e of transient bonds influences the nucleation, growth, and disappearance of condensed regions, or *clusters*, when ends are held at a fixed distance L_{sep} . Each simulated chain consists of 1600 beads with a diameter of $b = 0.01 \mu\text{m}$, resulting in a total contour length of $L_{tot} = 16 \mu\text{m}$. Clusters are identified using the DBSCAN algorithm (see Appendix), enabling us to quantify dynamic properties such as the number $N_c(t)$ and size distribution of clusters $P(\ell_i, t)$. We conduct a preliminary investigation into the effects of varying tail length, spring constant, number of tails per chain segment, and overall chain length. Given the computational expense of a comprehensive analysis across all parameters, we focused on a baseline parameter set that reflects behavior observed in previous *in vitro* experiments (see Table 1) [52, 53]. We then characterize the effect of binding affinity, which is an experimentally relevant variation.

Determinants of Polymer Clustering

To ensure that the averaged results are independent of initial configurations, the polymer chain is first set in a helical geometry with a fixed number of turns (Appendix). The chain is then evolved under Brownian fluctuations (without crosslinking) for $T = 100$ seconds, or $T/\tau_R \approx 1$, where $\tau_R = \frac{\eta b^3 N^2}{\pi k_B T}$ is the Rouse relaxation time. Twelve independent realizations of the system are averaged to obtain the final results, along with confidence intervals as shown in Fig. 2(A).

We first examine how the condensation dynamics depend on K_e and L_{sep} . Fig. 2(A) shows temporal courses of condensation, as measured by ℓ_{tot} , the total length of chain in clusters. It is only beyond a critical value of K_{e*} that clusters form, with ℓ_{tot} reaching a plateau for a given L_{sep} . Fig. 2(B) exhibits the phase transition behavior of the polymer chain by showing the fraction of the chain in clusters as a function of K_e and L_{sep} . Similar phase transitions from unclustered to clustered states are predicted by phenomenological models and observed in experimental studies [53, 52]. From Fig. 2(A,B), we determine the

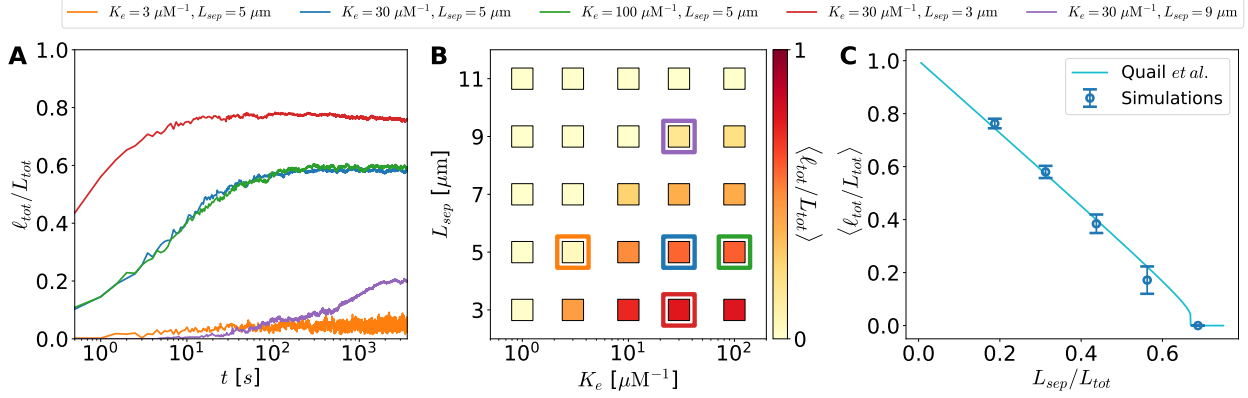


Figure 2: (A) Average values of total clustered chain length ℓ_{tot} normalized by L_{tot} . Curves represent averages over 12 independent realizations. Curve colors correspond to different values of K_e and L_{sep} , as indicated at the top of the figure. Shaded areas are 95% confidence intervals of the mean. (B) Equilibrium values of $\langle \ell_{tot}/L_{tot} \rangle$ for different values of K_e and L_{sep} . The and the colored boxes around data points correspond to the curves in (A). (C) Comparison of the total clustered chain length from our $K_e = 30 \mu\text{M}^{-1}$ simulations (dark blue) to previous equilibrium theories with experimentally inferred constants (cyan) [53, 52].

critical values of the microscopic parameters, $K_e^* = 1 \mu\text{M}^{-1}$ and $L_{sep}^* = 11 \mu\text{m}$, that determine the clustered state of a constrained chain at long times. Further details on how variations in K_e affect cluster dynamics are discussed in Sec. . Additionally, our results show that increasing the end-to-end separation L_{sep} slows clustering, as is evident from the comparison of the red, blue, and purple curves in Fig. 2(A).

Fig. 2(C) shows that the long-time behavior of ℓ_{tot} in simulations with $K_e = 30 \mu\text{M}^{-1}$ aligns well with the equilibrium model and parameters proposed and measured by Quail *et al.* to describe *in vitro* experiments [53, 52]. Their model relied on fitted, phenomenological parameters, such as surface tension and condensate free-energy density, to predict the likelihood of DNA-protein co-condensation (Fig. 2(C) cyan). These equilibrium theories describe the steady-state macroscopic properties of the system, such as ℓ_{tot} , but do not address the transient dynamics of clusters. Our approach captures both the macroscopic properties of the system and the cluster evolution. The agreement between our simulations and the equilibrium model suggests a correspondence between the microscopic and macroscopic parameters employed in both approaches. In the following sections, we explore how systems of clustering chains progress toward their steady-state configurations.

Spatiotemporal Dynamics of Cluster Evolution

During simulations, multiple clusters rapidly form along the chain at short times, eventually evolving toward a single cluster at longer timescales ($t \gg \tau_R$) as shown in Fig. 3(A,D). This dynamic behavior is consistent across all systems exhibiting clustering and has been previously observed in both free and constrained, potential-based polymer simulations [3, 61, 37, 67]. As we did for the equilibrium cluster states in section ,

we now wish to characterize how variations in K_e and L_{sep} influence the dynamics of individual clusters.

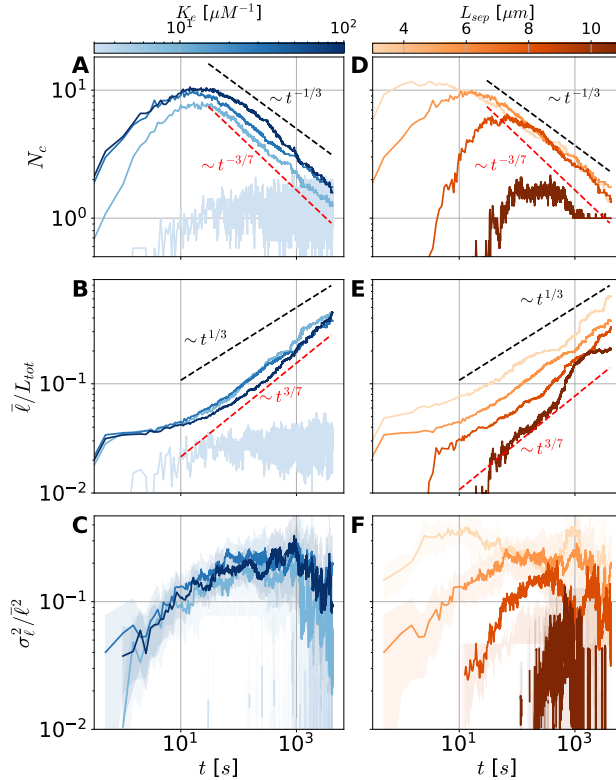


Figure 3: (A,D) Number of clusters N_c , (B,E) average cluster size $\bar{\ell}$, and (C,F) variance of clusters σ_{ℓ}^2 scaled by $\bar{\ell}^{-2}$ as functions of time. Curves are averaged over 12 realizations using different random number generator seeds. Shaded areas are 95% confidence intervals of the mean. (A-C) Parameter sets with $L_{sep} = 5 \mu\text{m}$ and varied binding affinities ($K_e = 3, 10, 30, 100 \mu\text{M}^{-1}$). (D-F) Parameter sets with $K_e = 30 \mu\text{M}^{-1}$ and varied end separations ($L_{sep} = 3, 5, 7, 9 \mu\text{m}$).

We first examine how the number of clusters evolves over time as a function of tail binding affinity. As previously mentioned, we observe distinct clustering regimes. At $K_e = 1 \mu\text{M}^{-1}$, no clustering occurs while at $K_e = 3 \mu\text{M}^{-1}$, transient individual clusters with short lifespans form. For higher binding affinities ($K_e \geq 10 \mu\text{M}^{-1}$), we observe that clusters nucleate and grow (see Fig. 12 in Appendix). For $K_e \geq 10 \mu\text{M}^{-1}$, the maximum number of nucleated clusters increases only modestly with higher binding affinity, as shown in Fig. 3(A).

Following the initial nucleation of clusters, we observe a universal decrease in cluster number over time, as shown in Fig. 3(A,D). The number of clusters appears to follow a power law $N_c \propto t^{-\mu}$ in this regime, with an exponent in the range $1/3 \leq \mu \leq 3/7$. Previous simulations using Lennard-Jones potentials by Aranson and Tsimring [3] showed a somewhat faster decrease in the number of clusters following $N_c \propto t^{-1/2}$. This behavior was attributed to the merging of clusters driven by diffusion along the chain backbone. However, the Aranson and Tsimring noted that cluster diffusion was likely overestimated due to the use of the Nose-Hoover

thermostat, which could bias the rate of cluster disappearance. This discrepancy in the scaling law for N_c between previous works and our simulations suggests the presence of additional mechanisms influencing the growth and disappearance of clusters. Interestingly, at longer times – when the total chain in clusters has plateaued >10 sec)– the cluster variance appears to scale with the average cluster size squared Fig. 3(C,F). This information proves helpful in deriving a theory to describe the evolution of cluster distributions.

Using free energy arguments to construct a minimal model, we explain the clustering dynamics observed in our simulations (see Appendix for details). We assume the rate at which chain segments enter clusters is determined by the balance between the tension exerted by clusters on unclustered chain sections (strands) and the viscous friction on the strands from the solvent. The force generated by cluster i on its adjacent strands is derived from the free energy of a cluster as

$$f_i = -\alpha + \gamma \ell_i^{-\frac{1}{3}}, \quad (9)$$

where α represents the cluster’s bulk energy and γ denotes the effective surface tension. Consequently, we determine that the growth rate of the average cluster size follows $\bar{\ell} \propto t^\mu$, where the exponent μ depends on the primary mechanism driving cluster evolution. Specifically, $\mu = 1/3$ corresponds to a merging-dominated regime, while $\mu = 3/7$ indicates a ripening-dominated regime, where ripening refers to the growth of some clusters at the expense of others shrinking and dissolving. The characteristic timescales for these two processes can be estimated as follows:

$$\tau_{merge} \cong \bar{s}^2 / \bar{D}_c, \quad \tau_{ripe} \cong \eta \bar{s} \bar{\ell}^{4/3} / \gamma, \quad (10)$$

where $\bar{D}_c \cong k_B T / \eta \bar{\ell}$ is the average diffusion constant of clusters and \bar{s} is the average length of the strands connecting clusters. Initially, when clusters are small and positioned closely along the chain, merging plays a dominant role. As the average strand length between clusters increases, the merging timescale, τ_{merge} —governed by one-dimensional diffusion along the backbone—grows and eventually increases beyond the timescale for ripening. Thus, ripening becomes the dominant mechanism, as $\tau_{ripe} < \tau_{merge}$.

Extending our analysis, we examine the average length of chain in clusters and in connecting strands, denoted by $\bar{\ell} = \ell_{tot} / N_c$ and $\bar{s} = s_{tot} / (N_c + 1) \approx s_{tot} / N_c$, respectively. These definitions imply a relationship between the average cluster size and the strand length, expressed as $\bar{s} \approx a \bar{\ell}$, where $a = s_{tot} / \ell_{tot}$. The total polymer length L_{tot} can be separated into the contributions from clusters and strands, yielding $L_{tot} = \ell_{tot} + s_{tot}$. Moreover, as illustrated in Fig. 2(C), we observe that the total length of clustered chains decreases nearly linearly with the end-to-end separation, following the relationship $\ell_{tot} \approx L_{tot} - c L_{sep}$, where c is

derived from Fig. 2(C) and is a function of K_e . From this, we infer that $s_{tot} \approx c L_{sep}$, leading to:

$$a = \frac{s_{tot}}{\ell_{tot}} \approx \left(\frac{L_{tot}}{c L_{sep}} - 1 \right)^{-1}, \quad (11)$$

where a is a function of L_{tot}, K_e and L_{sep} . From this relation, we may convert the timescales of equation (10) into functions of only \bar{s} , $\bar{\ell}$, or N_c , allowing for analytic comparison between timescales. For example, the relation highlights the difference between the ripening mechanism of cluster growth and that of typical Oswald ripening. By substituting $\bar{\ell}$ for \bar{s} in equation (10), one finds $\bar{\ell} \sim t^{3/7}$ through ripening alone. Assuming that clusters are roughly spherical, this scaling implies an average radius of clusters to scale as $\bar{R}_c \sim t^{1/7}$ as opposed to the classical Oswald ripening scaling of $\bar{R}_{Os} \sim t^{1/3}$.

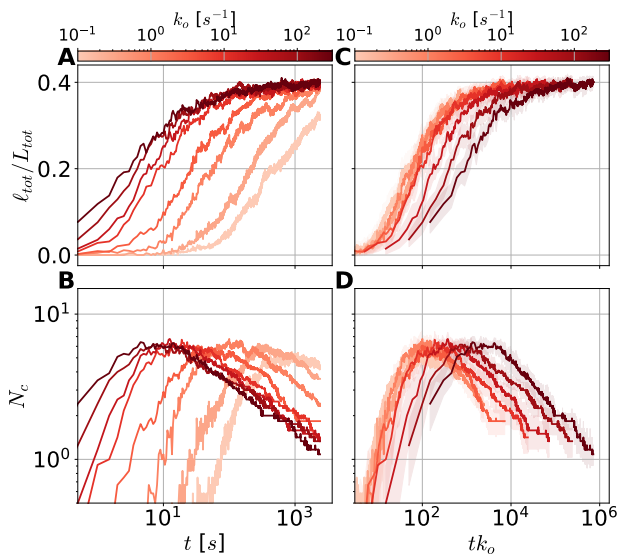


Figure 4: (A,C) Total chain in clusters and (B,D) number of clusters as functions of time with $K_e = 30\mu M^{-1}$, $L_{sep} = 5\mu m$, and varying crosslinker turnover rates ($k_o = .1, .3, 1, 3, 10, 30, 100, 300s^{-1}$). Curves are averaged over 12 independent realizations using different random number generator seeds. Shaded areas are 95% confidence intervals of the mean. In (A,B), time is in units of seconds whereas in (C,D), time is rescaled by the inverse of the crosslinker binding rate.

Next we investigate the effect of turnover rate, k_o , on system behavior (Fig. 4). The turnover rate proportionally scales both the binding and unbinding rates. Panels A, B in Fig. 4 demonstrate that increasing k_o leads to higher rates of cluster formation, faster initial cluster growth, and more rapid cluster disappearance at long times. However, the maximum length of all clusters, the maximum number of clusters, and the scaling behavior remain unchanged across all test cases. This confirms that these quantities are primarily governed by K_e and L_{sep} rather than k_o . Proportional changes in binding and unbinding rates alter the rate at which macroscopic properties, such as the number of clusters, evolve but do not necessarily affect the dominant mechanisms driving their evolution. Notably, for $k_o \geq 10 s$, the measured quantities ℓ_{tot}/L_{tot}

and N_c show similar behavior at times >10 sec roughly collapsing onto a single curve (Fig. 4(C,D)).

Conversely, when time is rescaled with k_o , simulations with $k_o < 10$ s also partially collapse onto a single curve, as shown in Fig. 4(C,D). This suggests a crossover in the relevant timescales. For slow crosslinking kinetics, cluster formation is reaction-limited. However, as crosslinking becomes faster, the system transitions to a regime limited by another mechanism. While several timescales are present in the system, the most likely limiting factor is the viscous drag of the chains. Notably, the Rouse time is unlikely to play a significant role in this crossover since the entire chain does not need to rearrange for individual clusters to evolve. Instead, the dynamics are governed by the motion of individual clusters and unclustered segments. The drag coefficient for clusters or segments scales proportionally with the number of beads they contain. Using the Stokes-Einstein relation, we estimate the diffusion timescale over a distance equal to the bead diameter as $\tau_d = 3\pi\eta\bar{\ell}b^2/k_B T$. For cluster or segment sizes on the order of 100 beads, this timescale is approximately 0.1 s, which is consistent with the critical turnover rate of $k_o \sim 10$ s⁻¹.

Cluster Lineage and Modes of Growth

While a minimal model, based on free energy arguments, successfully describes the growth dynamics of clusters, it provides only partial insight into the specific mechanisms governing cluster evolution and their relative significance. To understand aspects such as cluster lifetimes, size fluctuations, and movement in both positional and chain index space requires us to track individual clusters throughout their evolution. Hence, we developed a tracking algorithm, detailed in section , that reliably recognizes clusters over time. This approach facilitates a more detailed investigation of clusters' dynamic behavior.

Fig. 5(A) visualizes the evolution of clusters in the index space over time, showing the lineage of individual clusters. The corresponding cluster sizes, shown in Fig. 5(B), track their nucleation, growth, and disappearance over time. Using our algorithm, we determine whether a cluster disappears due to merging with another cluster or by gradually dissolving as beads dissociate. As is evident from Fig.5(A), a number of clusters initially nucleate randomly along the backbone. Many of them rapidly merge, forming larger clusters. At later times, $t > 100$ s, clusters not only migrate through positional space but also translocate along the polymer backbone as beads associate or dissociate (see Fig. 13 in Appendix). At these later times, we also observe ripening phenomena as cluster sizes change relatively slowly with larger clusters growing while the smaller clusters shrink and dissolve. The larger the difference between clusters, the more likely and more quickly the smaller cluster dissolves. Having looked at a single realization, now we discuss the statistical behavior of clusters.

The average cluster size, shown in Fig. 6(A), follows a scaling law, $\langle \ell_i \rangle \propto t^{0.35}$, consistent with the

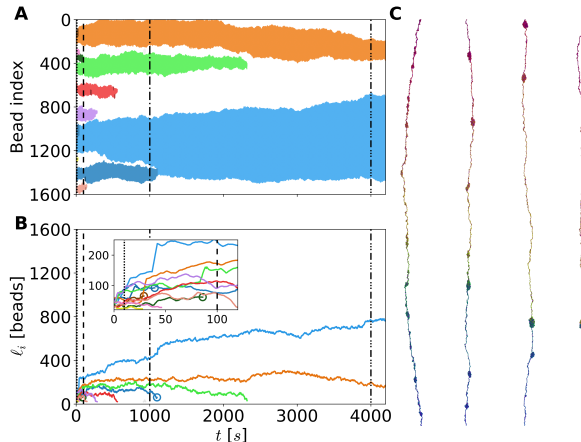


Figure 5: Visualization of cluster dynamics in a single simulation. (A) Clusters shown in bead index space over time. Filled regions of the same color indicate bead indices belonging to the same cluster, with darker shades representing earlier time points in the cluster’s genealogy. (B) Cluster sizes from (A) as a function of time, with merging events marked by circles. (Inset) Zoomed-in view of the first 100 seconds of (B). (C) 3D snapshot of the system at the time indicated by the dotted lines in (A) and (B).

theoretical bounds discussed in Section . Notably, this scaling behavior differs from that found in previous studies, where cluster growth was primarily driven by merging [3]. This led to an average cluster length scaling as $\langle \ell_i \rangle \propto t^{1/3}$, though it was acknowledged that the use of the Nose-Hoover integration method resulted in artificially high cluster diffusion [3]. The authors of [3] argued that in a minimal model, incorporating realistic local drag would alter the cluster size scaling to $\langle \ell_i \rangle \propto t^{3/7}$. Our work provides a physical foundation for this scaling law, associating it with a regime where ripening is the dominant growth mechanism.

Fig. 6(B) compares the histograms of merging and dissolving events over time. In the first 20 seconds of the simulation, very few dissolving events occur. During this period, the small clusters would only experience weak tension from the excess chain between clusters, allowing clusters to grow unhindered. Ripening begins in earnest only after the total chain length in clusters, ℓ_{tot} , plateaus and unclustered chain segments become stretched. As time progresses, the average distance between clusters increases, making dissolving events more frequent than merging.

Throughout most of the transient evolution of clusters in our simulations dissolving and merging events occur at comparable rates. At later times, both kinds of termination events become less frequent, though merging becomes less prevalent. There is little to no nucleation of new clusters at long times. From a free energy perspective, nucleating a new cluster would require overcoming a significant energy barrier, either by stretching the chain or reducing the size of existing clusters to accommodate a new cluster that does not immediately dissolve. Overall, ripening events occur at a rate 1.43 times that of merging events, though the mean dissolving time, $\langle t_D \rangle = 428$ s, is longer than the mean merging time, $\langle t_M \rangle = 206$ s.

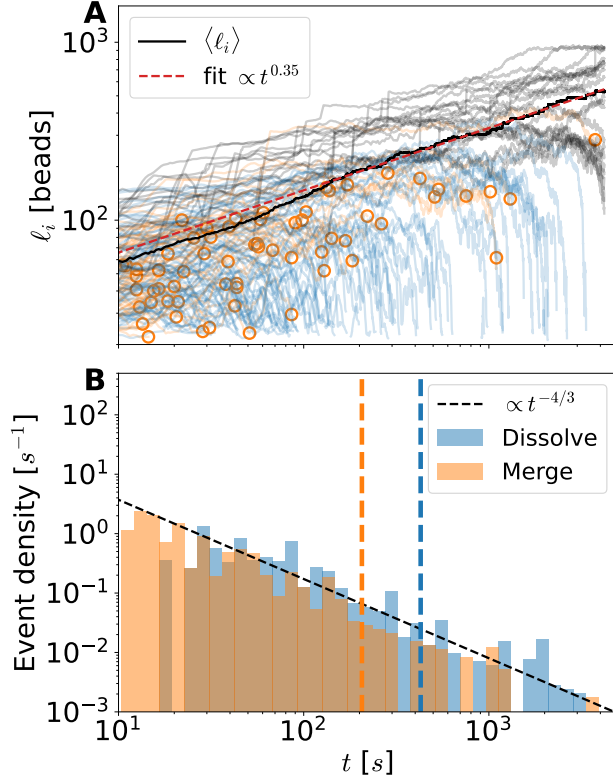


Figure 6: (A) Size traces of all clusters plotted as a function of time for systems with $L_{sep} = 5\mu m$, $K_e = 30\mu M^{-1}$, and $k_o = 3s^{-1}$. Trace color indicates cluster fate: blue for dissolving, orange for merging, and gray for clusters that persist until the end of the simulation. Orange circles mark merging events. The average cluster size is plotted as a black line, fitted to a power law $\langle \ell_i \rangle = at^b$ with $a = 29.37$, $b = .35$ and $r^2 = .9905$ (red dashed line). (B) Histogram of dissolving (blue) and merging (orange) event times from (A). The mean merging time $\langle t_M \rangle = 206$ s (dashed orange line) and mean dissolving time $\langle t_D \rangle = 428$ s (dashed blue line) are shown along with the predicted scaling behavior (dashed black line). Proportion of events: dissolving $p_D = 0.59$ and merging $p_M = .41$.

Since fewer clusters exist at later times, drawing convincing conclusions about long-term cluster growth modes is challenging. To analyze late-time behavior in more detail, we initialized simulations with two identically sized preformed clusters separated by an unclustered chain segment of approximately 100 beads (6% of all beads), as shown in Fig. 7. The initial cluster sizes were chosen so that the total chain length in clusters matched the steady-state value found in Section .

We observed that the segment length separating the clusters influenced both dissolving and merging rates. Notably, when clusters were initialized with three equal-length strands, no merging or dissolving events occurred within the first 1200 s (data not shown). However, reducing the strand length between clusters to 100 beads increased the frequency of events, consistent with our estimates that predict $\tau_{merge} \sim s^2\bar{\ell}$ and $\tau_{ripen} \sim s\bar{\ell}^{4/3}$ from section .

We find that ripening is the dominant mode of cluster evolution in these simulations ($p_r = 63.9$). The

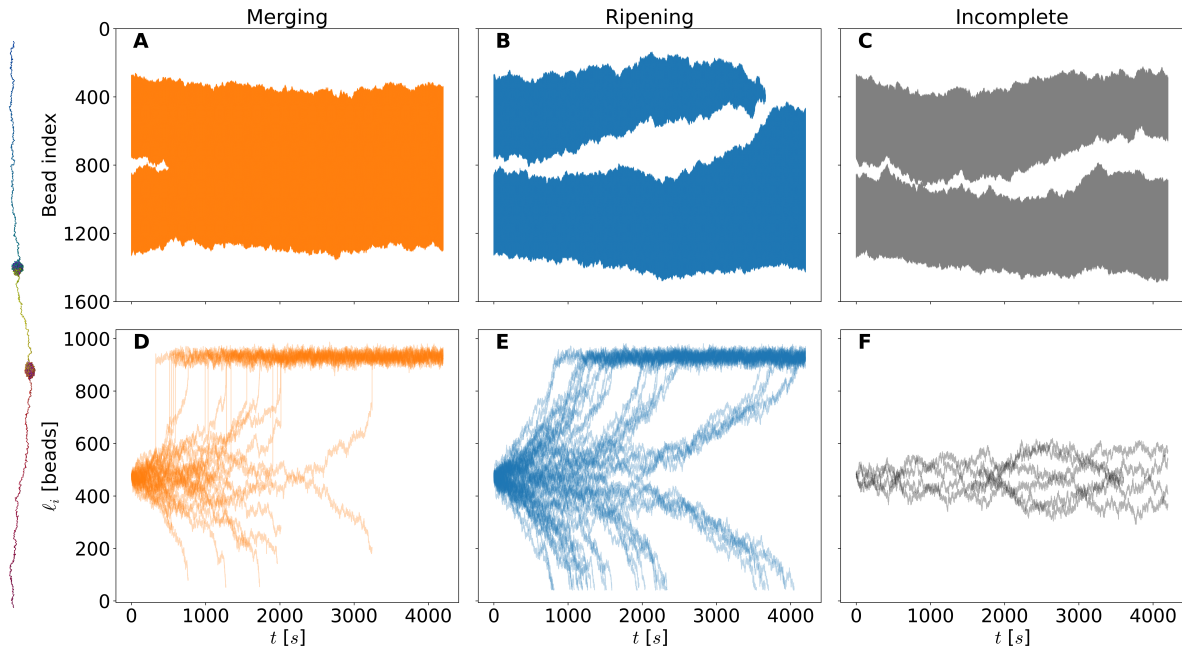


Figure 7: Time evolution of equal-sized clusters separated by 100 beads, with $L_{sep} = 5\mu m$, $K_e = 30\mu M^{-1}$, and $k_o = 3s^{-1}$, across 48 replicated simulations. (Far left) Example of the initial configuration in 3D. (A–C) Representative examples of clustered bead indices over time for (A) merging events, (B) ripening events, and (C) cases where no events occur. (D–F) Cluster size as a function of time for all replicates undergoing (D) merging events ($N_M = 17$), (E) ripening (dissolving) events ($N_D = 28$), and (F) no events ($N_{NE} = 3$).

majority of dissolving events took place when the segment between two clusters consisted of only a few tens of beads, highlighting the total viscous drag acting on the connecting segment governs the rate at which one cluster absorbs chain from another. During ripening, the segment between clusters moved superdiffusively in index space, while the cluster edges not adjacent to the segment (the outer segments) remained nearly fixed. This behavior further supports the primary assumption of our minimal model for ripening—that the sizes of the outer pinned segments remain relatively unchanged compared to the segment between clusters.

Ripening events occurred with seemingly random distribution. However, aligning all ripening events relative to the time of complete ripening, $t' = t - t_r$, reveals a consistent trajectory, as shown in Fig. 8. Our minimal model predicts that the cluster size near total ripening follows

$$\ell(t) \approx \left(\ell_o^{4/3} - \frac{4t}{3\tau} \right)^{3/4}, \quad (12)$$

to leading order, where $\tau = 3\pi\eta\ell_{tot}^{1/3}s/\gamma$ is the timescale set by the strand being incorporated into the larger condensate (see Appendix). Notably, the dissolving time, defined by $\ell(t_{diss}) = 0$, depends on the initial difference in cluster sizes. While the simulations were initialized with identical cluster sizes, our results

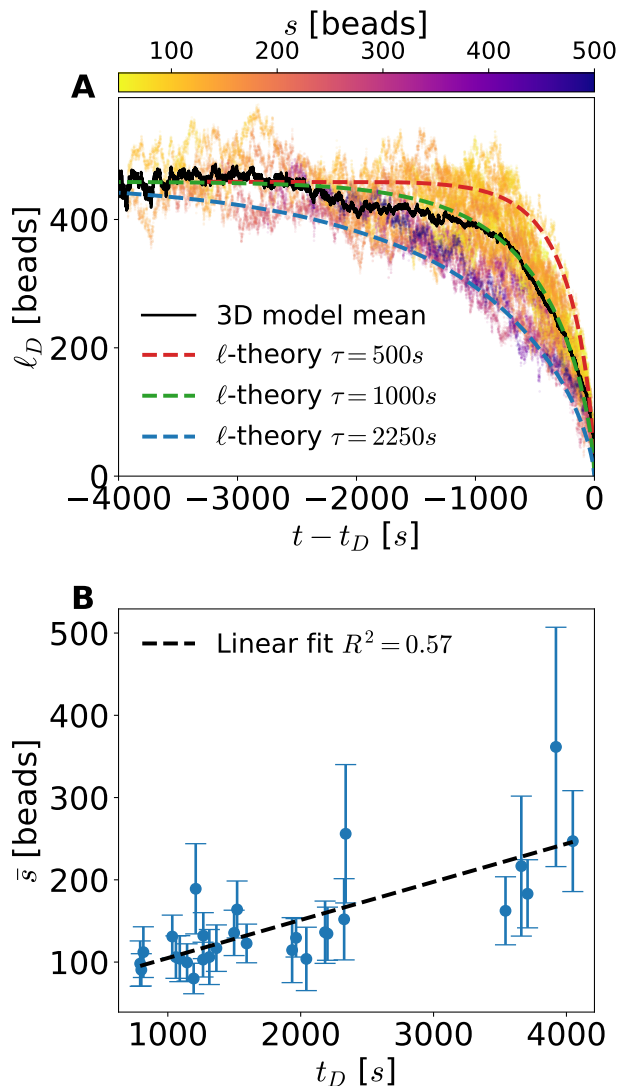


Figure 8: Effect of strand length on the size evolution of dissolving clusters. (A) Synchronized cluster size traces for 28 dissolving clusters from Fig. 7(E). The size traces are temporally aligned such that the ripening time $t_d = 0$. Line color indicates the instantaneous length of the strand separating the clusters. The black line represents the ensemble average cluster size. Predicted trajectories from theory (Appendix) for three different time constants ($\tau = 500, 1000, 2250$ s) are shown by dashed lines. (B) Time-averaged strand size of dissolving simulations as a function of ripening time with error bars showing standard deviation of strand size over run. Black dotted line is a least-squares linear fit $\bar{s}_{fit} = at_D + b$ with $a = .043$ and $b = 58.6$.

indicate that fluctuations in cluster size are sufficient to create imbalances in the forces acting on clusters, ultimately driving ripening. This explains the distribution of dissolving events, as cluster size differences emerge through a stochastic process.

Discussion

In this study, we investigated how fundamental microscopic parameters governing crosslinking influence the condensation of a constrained polymer. We demonstrated a transition from a non-clustering to a clustering phase as a function of binding affinity K_e and polymer end-to-end separation L_{sep} . Within the clustering phase, after initial nucleation and cluster growth, the amount of chain incorporated into clusters reaches a steady state. Beyond this point, the number of clusters decreases through two primary mechanisms: merging (coalescence) and dissolving (ripening). Using a minimal model based on free energy and mechanical arguments, we identified distinct timescales associated with each mechanism. Our results demonstrate that the competition between these two processes dictates the observed scaling behavior in our simulations.

Among the microscopic parameters examined, it is L_{sep} and K_e that primarily determine macroscopic properties such as the maximum number of clusters and the total chain length within clusters. In contrast, the turnover rate of crosslinkers, k_o , does not affect these macroscopic properties or the system’s scaling behavior but instead controls the rate at which these quantities evolve. Our analysis suggests that varying the turnover rate proportionally alters the timescales of merging and dissolving without affecting their relative competition. Beyond a critical turnover rate, the system’s dynamics become limited by the diffusive timescale associated with the motion of clusters and chain segments within the viscous medium.

To further investigate the interactions between clusters mediated by connecting segments, we analyzed a system with two identically sized clusters separated by a short connecting segment ($\sim 6\%$ of the total chain length). Transient fluctuations in cluster sizes created imbalances in the forces acting on the clusters, which in turn triggered ripening. Unlike simulations that began with unclustered chains, these systems predominantly exhibited ripening as the primary mode of cluster evolution. Consistent with our minimal model and scaling arguments, we found that the cluster ripening is linearly proportional to the length of the segment connecting neighboring clusters. Moreover, we observe that dissolving of a cluster follows a deterministic trajectory. Using our minimal model, we provide a general ODE framework with a single free parameter that effectively sets the timescale for this trajectory toward total dissolution. This timescale is governed by the surface tension γ of clusters in our phenomenological model. While our study focuses on a specific sticky-tail polymer condensation model, the underlying theory of cluster ripening applies broadly to any constrained homopolymer with attractive interactions.

These findings have broader implications for biological systems, particularly chromatin organization within the nucleus. Given that cluster formation on a constrained polymer chain can take tens of minutes to hours, such timescales may be too slow for genomic processes such as transcriptional enhancement or silencing. This raises the possibility that long-range hydrodynamic interactions play a role in accelerat-

ing chromatin clustering [78, 21, 32]. Indeed, active hydrodynamic forces have been proposed to stir the nucleoplasm and enhance chromatin condensation [56, 77, 39]. A natural extension of our work would be to incorporate these interactions and explore how different sources of activity—such as forces generated by loop-extruding factors, polymerases, and topoisomerases—affect chromatin organization. Furthermore, sequence-dependent condensation and segregation have been observed in both *in vitro* and *in vivo* studies [43, 46, 60]. Variations in DNA-binding affinities could significantly influence cluster dynamics, potentially accelerating collapse while ensuring that critical genes remain transcriptionally active, thereby preventing unintended silencing.

Acknowledgments

The authors thank support from NSF grants DMR-2004469 and CMMI-1762506. The computations in this work were performed at facilities supported by the Scientific Computing Core at the Flatiron Institute, a division of the Simons Foundation.

Table 1: Summary of parameters for 3D simulations. System parameters are constant values used in simulations from previously known or measured values. Assay values were chosen to match experiments that employed λ -DNA [52, 53, 43]. Microscopic model parameters determined the behavior of the sticky tails and existed within physiologically relevant ranges. These were scanned over to identify values at which condensates would form. Simulation parameters were chosen to provide long-time behavior without compromising accuracy. Parameters used in free-energy models are shown under coarse-grained parameters.

Parameter	Symbol	Value	Reference
System parameters			
Bead (nucleosome) diameter	b	10 nm	Well known
Diameter of amino acid	b_{amino}	0.4 nm to 1 nm	Well known
dsDNA persistence length	l_p	50 nm	Well known
ssDNA persistence length	$l_{p,ss}$	2.2 nm	Chi et al.[10]
IDR persistence length	$l_{p,idp}$	0.4 nm to 0.5 nm	Hofmann et al.[25]
Nucleotide length	b_n	0.34 nm	Well known
Nucleotides in linker DNA	N_{link}	45	Alberts et al.[1]
Double stranded DNA force plateau	f_{ds}	65 pN	Kumar et al. [35]
Maximum extension of dsDNA	ϵ_{max}	1.7	Kumar et al. [35]
DNA linker spring constant	κ_{DNA}	4 pN nm ⁻¹	Calculated
Thermal energy	$k_B T$	4.11 pN nm	Well known
Solvent viscosity	η	1 pN s μm^{-2}	Cytoplasm viscosity, Well known
Assay values			
Length of chain	L	16.5 μm	Quail et al. [52]
Number of beads	N	1650	Calculated
Pinned distance	L_d	2 μm to 10 μm	Chosen [52]
Microscopic binding parameters			
Kinetic rate	k_o	3 s ⁻¹	Chosen (values range from 0.1–300)
Sticky end equilibrium constant	K_e	30 μM^{-1}	Chosen (values range from 0.1–300)
Binding site density	λ_s	1	Subsumed into K_e
Sticky end spring constant	κ_s	800 pN μm^{-1}	Calculated from FUS IDR values [28]
Sticky end length	l_x	0.005 μm	Calculated from FUS IDR values [28]
Simulation parameters			
Timestep	Δt	1 $\times 10^{-4}$ s	Chosen for accuracy, stability, and efficiency
Coarse-grained parameters			
Condensation free energy per volume	μ	4.1 pN μm^{-1} to 11.9 pN μm^{-1}	Renger et al. [53]
Condensate packing factor	α	0.05 μm^2 to 0.06 μm^2	Renger et al. [53]
Condensate surface tension	γ	0.15 pN μm^{-1}	Renger et al. [53]
Filament flexibility	$k_B T/l_p$	0.0822 pN	Calculated

References

- [1] Bruce Alberts, Alexander Johnson, Julian Lewis, David Morgan, Martin Raff, Keith Roberts, and Peter Walter. *Molecular Biology of the Cell*. W.W. Norton and Company, aug 2017.
- [2] Daria Amiad-Pavlov, Dana Lorber, Gaurav Bajpai, Adriana Reuveny, Francesco Roncato, Ronen Alon, Samuel Safran, and Talila Volk. Live imaging of chromatin distribution reveals novel principles of nuclear architecture and chromatin compartmentalization. *Science Advances*, 7(23):6251–6253, jun 2021.
- [3] I. S. Aranson and L. S. Tsimring. Dynamics of the constrained polymer collapse. *Europhysics Letters (EPL)*, 62(6):848–854, jun 2003.
- [4] Amandine Barral and Kenneth S. Zaret. Pioneer factors: roles and their regulation in development. *Trends in Genetics*, 40(2):134–148, feb 2024.
- [5] Yashar Bashirzadeh, Steven A. Redford, Chatipat Lorpaiboon, Alessandro Groaz, Hossein Moghimi-anavval, Thomas Litschel, Petra Schwille, Glen M. Hocky, Aaron R. Dinner, and Allen P. Liu. Actin crosslinker competition and sorting drive emergent GUV size-dependent actin network architecture. *Communications Biology* 2021 4:1, 4(1):1–11, sep 2021.
- [6] Clifford P. Brangwynne, Peter Tompa, and Rohit V. Pappu. Polymer physics of intracellular phase transitions. *Nature Physics* 2015 11:11, 11(11):899–904, nov 2015.
- [7] Guy Bunin and Mehran Kardar. Coalescence Model for Crumpled Globules Formed in Polymer Collapse. *Physical Review Letters*, 115(8):088303, aug 2015.
- [8] Xue Zheng Cao and M. Gregory Forest. Rheological Tuning of Entangled Polymer Networks by Transient Cross-links. *Journal of Physical Chemistry B*, 123(5):974–982, feb 2019.
- [9] Keerti Chauhan and Ankit Singh. Delayed collapse transitions in a pinned polymer system. *Physical Review E*, 105(6):064505, jun 2022.
- [10] Qingjia Chi, Guixue Wang, and Jiahuan Jiang. The persistence length and length per base of single-stranded DNA obtained from fluorescence correlation spectroscopy measurements using mean field theory. *Physica A: Statistical Mechanics and its Applications*, 392(5):1072–1079, mar 2013.
- [11] Won Ki Cho, Jan Hendrik Spille, Micca Hecht, Choongman Lee, Charles Li, Valentin Grube, and Ibrahim I. Cisse. Mediator and RNA polymerase II clusters associate in transcription-dependent condensates. *Science*, 361(6400):412–415, jul 2018.

- [12] P. G. de Gennes. Kinetics of collapse for a flexible coil. *Journal de Physique Lettres*, 46(14):639–642, jul 1985.
- [13] Dafne Campigli Di Giammartino, Alexander Polyzos, and Effie Apostolou. Transcription factors: building hubs in the 3D space. *Cell Cycle*, 19(19):2395–2410, oct 2020.
- [14] Serge Dmitrieff, Adolfo Alsina, Aastha Mathur, and François J. Nédélec. Balance of microtubule stiffness and cortical tension determines the size of blood cells with marginal band across species. *Proceedings of the National Academy of Sciences of the United States of America*, 114(17):4418–4423, apr 2017.
- [15] Martin Ester, Hans-Peter Kriegel, Jiirg Sander, and Xiaowei Xu. A Density-Based Algorithm for Discovering Clusters in Large Spatial Databases with Noise. 1996.
- [16] Tobias T. Falzone, Martin Lenz, David R. Kovar, and Margaret L. Gardel. Assembly kinetics determine the architecture of α -actinin crosslinked F-actin networks. *Nature Communications 2012 3:1*, 3(1):1–9, may 2012.
- [17] Celestia Fang, Sridhar Rao, John D. Crispino, and Panagiotis Ntziachristos. Determinants and role of chromatin organization in acute leukemia. *Leukemia 2020 34:10*, 34(10):2561–2575, jul 2020.
- [18] Lukas Frank and Karsten Rippe. Repetitive RNAs as Regulators of Chromatin-Associated Subcompartment Formation by Phase Separation. *Journal of Molecular Biology*, 432(15):4270–4286, jul 2020.
- [19] Giovanni Gambi, Francesco Boccalatte, Javier Rodriguez Hernaez, Ziyang Lin, Bettina Nadorp, Alexander Polyzos, Jimin Tan, Kleopatra Avramou, Giorgio Inghirami, Alex Kentsis, Effie Apostolou, Iannis Aifantis, and Aristotelis Tsigos. 3D chromatin hubs as regulatory units of identity and survival in human acute leukemia. *Molecular Cell*, 85(1):42–60.e7, jan 2025.
- [20] Stefan Golfier, Thomas Quail, Hiroshi Kimura, and Jan Brugués. Cohesin and condensin extrude DNA loops in a cell-cycle dependent manner. *eLife*, 9:1–34, may 2020.
- [21] A. Halperin and Paul M. Goldbart. Early stages of homopolymer collapse. *Physical Review E*, 61(1):565–573, jan 2000.
- [22] A. Halperin and E. B. Zhulina. On the Deformation Behaviour of Collapsed Polymers. *Europhysics Letters*, 15(4):417, jun 1991.
- [23] Jonathan E. Henninger, Ozgur Oksuz, Krishna Shrinivas, Ido Sagi, Gary LeRoy, Ming M. Zheng, J. Owen Andrews, Alicia V. Zamudio, Charalampos Lazaris, Nancy M. Hannett, Tong Ihn Lee, Phillip A.

- Sharp, Ibrahim I. Cissé, Arup K. Chakraborty, and Richard A. Young. RNA-Mediated Feedback Control of Transcriptional Condensates. *Cell*, 184(1):207–225.e24, jan 2021.
- [24] Claire Hoencamp and Benjamin D. Rowland. Genome control by SMC complexes. *Nature Reviews Molecular Cell Biology* 2023 24:9, 24(9):633–650, may 2023.
- [25] Hagen Hofmann, Andrea Soranno, Alessandro Borgia, Klaus Gast, Daniel Nettels, and Benjamin Schuler. Polymer scaling laws of unfolded and intrinsically disordered proteins quantified with single-molecule spectroscopy. *Proceedings of the National Academy of Sciences*, 109(40):16155–16160, 2012.
- [26] Tsung Han S. Hsieh, Claudia Cattoglio, Elena Slobodyanyuk, Anders S. Hansen, Oliver J. Rando, Robert Tjian, and Xavier Darzacq. Resolving the 3D Landscape of Transcription-Linked Mammalian Chromatin Folding. *Molecular Cell*, 78(3):539–553.e8, may 2020.
- [27] Caitlin Hult, David Adalsteinsson, Paula A. Vasquez, Josh Lawrimore, Maggie Bennett, Alyssa York, Diana Cook, Elaine Yeh, Mark Gregory Forest, and Kerry Bloom. Enrichment of dynamic chromosomal crosslinks drive phase separation of the nucleolus. *Nucleic Acids Research*, 45(19):11159–11173, nov 2017.
- [28] Masato Kato and Steven L. McKnight. The low-complexity domain of the FUS RNA binding protein self-assembles via the mutually exclusive use of two distinct cross- β cores. *Proceedings of the National Academy of Sciences of the United States of America*, 118(42):e2114412118, oct 2021.
- [29] Madeline M. Keenen, David Brown, Lucy D. Brennan, Roman Renger, Harrison Khoo, Christopher R. Carlson, Bo Huang, Stephan W. Grill, Geeta J. Narlikar, and Sy Redding. HP1 proteins compact DNA into mechanically and positionally stable phase separated domains. *eLife*, 10, mar 2021.
- [30] Nimish Khanna, Yaojun Zhang, Joseph S. Lucas, Olga K. Dudko, and Cornelis Murre. Chromosome dynamics near the sol-gel phase transition dictate the timing of remote genomic interactions. *Nature Communications* 2019 10:1, 10(1):1–13, jun 2019.
- [31] Andreas Kloetgen, Palaniraja Thandapani, Panagiotis Ntziachristos, Yohana Ghebrechristos, Sofia Nomikou, Charalampos Lazaris, Xufeng Chen, Hai Hu, Sofia Bakogianni, Jingjing Wang, Yi Fu, Francesco Boccalatte, Hua Zhong, Elisabeth Paietta, Thomas Trimarchi, Yixing Zhu, Pieter Van Vlierberghe, Giorgio G. Inghirami, Timothee Lionnet, Iannis Aifantis, and Aristotelis Tsirigos. Three-dimensional chromatin landscapes in T cell acute lymphoblastic leukemia. *Nature Genetics*, 52(4):388–400, mar 2020.
- [32] L. I. Klushin. Kinetics of a homopolymer collapse: Beyond the Rouse–Zimm scaling. *The Journal of Chemical Physics*, 108(18):7917–7920, may 1998.

- [33] Nils Krietenstein, Sameer Abraham, Sergey V. Veney, Nezar Abdennur, Johan Gibcus, Tsung Han S. Hsieh, Krishna Mohan Parsi, Liyan Yang, René Maehr, Leonid A. Mirny, Job Dekker, and Oliver J. Rando. Ultrastructural Details of Mammalian Chromosome Architecture. *Molecular Cell*, 78(3):554–565.e7, may 2020.
- [34] Anton Krumm and Zhijun Duan. Understanding the 3D genome: Emerging impacts on human disease. *Seminars in Cell and Developmental Biology*, 90:62–77, jun 2019.
- [35] Sanjay Kumar and Mai Suan Li. Biomolecules under mechanical force. *Physics Reports*, 486(1-2):1–74, jan 2010.
- [36] Adam R. Lamson, Jeffrey M. Moore, Fang Fang, Matthew A. Glaser, Michael J. Shelley, and Meredith D. Betterton. Comparison of explicit and mean-field models of cytoskeletal filaments with crosslinking motors. *The European Physical Journal E 2021 44:3*, 44(3):1–22, mar 2021.
- [37] Anna Lappala and Eugene M. Terentjev. “Raindrop” Coalescence of Polymer Chains during Coil–Globule Transition. *Macromolecules*, 46(3):1239–1247, feb 2013.
- [38] Lunna Li, Matteo Paloni, Aaron R. Finney, Alessandro Barducci, and Matteo Salvalaglio. Nucleation of Biomolecular Condensates from Finite-Sized Simulations. *Journal of Physical Chemistry Letters*, 14(7):1748–1755, feb 2023.
- [39] Achal Mahajan, Wen Yan, Alexandra Zidovska, David Saintillan, and Michael J. Shelley. Euchromatin Activity Enhances Segregation and Compaction of Heterochromatin in the Cell Nucleus. *Physical Review X*, 12(4):041033, oct 2022.
- [40] Suman Majumder and Wolfhard Janke. Cluster coarsening during polymer collapse: Finite-size scaling analysis. *Europhysics Letters*, 110(5):58001, jun 2015.
- [41] Erik W. Martin, Alex S. Holehouse, Ivan Peran, Mina Farag, J. Jeremias Incicco, Anne Bremer, Christy R. Grace, Andrea Soranno, Rohit V. Pappu, and Tanja Mittag. Valence and patterning of aromatic residues determine the phase behavior of prion-like domains. *Science*, 367(6478):694–699, feb 2020.
- [42] Davide Michieletto and Mattia Marenza. Rheology and Viscoelasticity of Proteins and Nucleic Acids Condensates. *JACS Au*, 2(7):1506–1521, jul 2022.
- [43] Jose A. Morin, Sina Wittmann, Sandeep Choubey, Adam Klosin, Stefan Golfier, Anthony A. Hyman, Frank Jülicher, and Stephan W. Grill. Sequence-dependent surface condensation of a pioneer transcription factor on DNA. *Nature Physics 2022*, pages 1–6, feb 2022.

- [44] Fernando Muzzopappa, Maud Hertzog, and Fabian Erdel. DNA length tunes the fluidity of DNA-based condensates. *Biophysical Journal*, 120(7):1288–1300, apr 2021.
- [45] Takashi Nagano, Yaniv Lubling, Csilla Várnai, Carmel Dudley, Wing Leung, Yael Baran, Netta Mendelson Cohen, Steven Wingett, Peter Fraser, and Amos Tanay. Cell-cycle dynamics of chromosomal organization at single-cell resolution. *Nature*, 547(7661):61–67, jul 2017.
- [46] Tuan Nguyen, Sai Li, Jeremy T.H. Chang, John W. Watters, Htet Ng, Adewola Osunsade, Yael David, and Shixin Liu. Chromatin sequesters pioneer transcription factor Sox2 from exerting force on DNA. *Nature Communications* 2022 13:1, 13(1):1–11, jul 2022.
- [47] Jeremy A. Owen, Dino Osmanović, and Leonid Mirny. Design principles of 3D epigenetic memory systems. *Science*, 382(6672), nov 2023.
- [48] George V. Papamokos, George Tziatzos, Dimitrios G. Papageorgiou, Spyros D. Georgatos, Anastasia S. Politou, and Efthimios Kaxiras. Structural Role of RKS Motifs in Chromatin Interactions: A Molecular Dynamics Study of HP1 Bound to a Variably Modified Histone Tail. *Biophysical Journal*, 102(8):1926, apr 2012.
- [49] Sharon Peppenella, Kevin J. Murphy, and Jeffrey J. Hayes. Intra- and inter-nucleosome interactions of the core histone tail domains in higher-order chromatin structure. *Chromosoma*, 123(1-2):3–13, mar 2014.
- [50] Frédéric Pontvianne, Marie Christine Carpentier, Nathalie Durut, Veronika Pavlišťová, Karin Jaške, Šárka Schořová, Hugues Parrinello, Marine Rohmer, Craig S. Pikaard, Miloslava Fojtová, Jiří Fajkus, and Julio Sáez-Vásquez. Identification of Nucleolus-Associated Chromatin Domains Reveals a Role for the Nucleolus in 3D Organization of the *A. thaliana* Genome. *Cell Reports*, 16(6):1574–1587, aug 2016.
- [51] William H Press and Marc Davis. HOW TO IDENTIFY AND WEIGH VIRIALIZED CLUSTERS OF GALAXIES IN A COMPLETE REDSHIFT CATALOG 1. 449P *The Astrophysical Journal*, 259:449–473, 1982.
- [52] Thomas Quail, Stefan Golfier, Maria Elsner, Keisuke Ishihara, Vasanthanarayan Murugesan, Roman Renger, Frank Jülicher, and Jan Brugués. Force generation by protein–DNA co-condensation. *Nature Physics*, 17(9):1007–1012, sep 2021.
- [53] Roman Renger, Jose A. Morin, Regis Lemaitre, Martine Ruer-Gruss, Frank Jülicher, Andreas Hermann, and Stephan W. Grill. Co-condensation of proteins with single- and double-stranded DNA. *Proceedings of the National Academy of Sciences of the United States of America*, 119(10), mar 2022.

- [54] Vicente Rodriguez-Gomez, Shy Genel, Mark Vogelsberger, Debora Sijacki, Annalisa Pillepich, Laura V Sales, Paul Torrey, Greg Snyder, Dylan Nelson, Volker Springel, Chung-Pei Ma, and Lars Hernquist. The merger rate of galaxies in the Illustris simulation: a comparison with observations and semi-empirical models. *MNRAS*, 449:49–64, 2015.
- [55] Benjamin R. Sabari, Alessandra Dall’Agnese, and Richard A. Young. Biomolecular Condensates in the Nucleus. *Trends in biochemical sciences*, 45(11):961, nov 2020.
- [56] David Saintillan, Michael J. Shelley, and Alexandra Zidovska. Extensile motor activity drives coherent motions in a model of interphase chromatin. *Proceedings of the National Academy of Sciences*, 115(45):11442–11447, nov 2018.
- [57] Serena Sanulli and Geeta J. Narlikar. Liquid-like interactions in heterochromatin: Implications for mechanism and regulation. *Current Opinion in Cell Biology*, 64:90–96, jun 2020.
- [58] Jan Schnatwinkel and Christian Herrmann. The interaction strength of an intrinsically disordered protein domain with its binding partner is little affected by very different cosolutes. *Physical Chemistry Chemical Physics*, 22(47):27903–27911, dec 2020.
- [59] E. M. Sevick, P. A. Monson, and J. M. Ottino. Monte Carlo calculations of cluster statistics in continuum models of composite morphology. *The Journal of Chemical Physics*, 88(2):1198–1206, jan 1988.
- [60] Krishna Shrinivas, Benjamin R. Sabari, Eliot L. Coffey, Isaac A. Klein, Ann Boija, Alicia V. Zamudio, Jurian Schuijers, Nancy M. Hannett, Phillip A. Sharp, Richard A. Young, and Arup K. Chakraborty. Enhancer Features that Drive Formation of Transcriptional Condensates. *Molecular Cell*, 75(3):549–561.e7, aug 2019.
- [61] Rohit Kumar Singh, Pinaki Swain, Mahipal Ganji, and Sandeep Choubey. Decoding the role of DNA sequence on protein-DNA co-condensation. *bioRxiv*, page 2024.02.24.581870, feb 2024.
- [62] Andrea Soranno, J. Jeremías Incicco, Paolo De Bona, Eric J. Tomko, Eric A. Galburt, Alex S. Holehouse, and Roberto Galletto. Shelterin components modulate nucleic acids condensation and phase separation. *bioRxiv*, page 2021.04.30.442189, apr 2021.
- [63] Volker Springel, Simon D.M. White, Giuseppe Tormen, and Guinevere Kauffmann. Populating a cluster of galaxies - I. Results at $z = 0$. *Monthly Notices of the Royal Astronomical Society*, 328(3):726–750, dec 2001.

- [64] Hilmar Strickfaden, Thomas O. Tolsma, Ajit Sharma, D. Alan Underhill, Jeffrey C. Hansen, and Michael J. Hendzel. Condensed Chromatin Behaves like a Solid on the Mesoscale In Vitro and in Living Cells. *Cell*, 183(7):1772–1784.e13, dec 2020.
- [65] Amy R. Strom, Yoonji Kim, Hongbo Zhao, Yi-Che Chang, Natalia D. Orlovsky, Andrej Košmrlj, Cornelis Storm, and Clifford P. Brangwynne. Condensate interfacial forces reposition DNA loci and probe chromatin viscoelasticity. *Cell*, 187(19):5282–5297.e20, sep 2024.
- [66] Mingxuan Sun, Hossein Amiri, Alexander B. Tong, Keishi Shintomi, Tatsuya Hirano, Carlos Bustamante, and Rebecca Heald. Monitoring the compaction of single DNA molecules in *Xenopus* egg extract in real time. *Proceedings of the National Academy of Sciences*, 120(12):2017, mar 2023.
- [67] Ryota Takaki, Yahor Savich, Jan Brugués, and Frank Jülicher. Active Loop Extrusion guides DNA-Protein Condensation. jul 2024.
- [68] Kensal E. van Holde. *Chromatin*. Springer Series in Molecular Biology. Springer New York, New York, NY, 1989.
- [69] Benjamin Walker, Dane Taylor, Josh Lawrimore, Caitlin Hult, David Adalsteinsson, Kerry Bloom, and M. Gregory Forest. Transient crosslinking kinetics optimize gene cluster interactions. *PLoS computational biology*, 15(8), 2019.
- [70] Jie Wang, Jeong Mo Choi, Alex S. Holehouse, Hyun O. Lee, Xiaojie Zhang, Marcus Jahnel, Shovamayee Maharana, Régis Lemaitre, Andrei Pozniakovsky, David Drechsel, Ina Poser, Rohit V. Pappu, Simon Alberti, and Anthony A. Hyman. A Molecular Grammar Governing the Driving Forces for Phase Separation of Prion-like RNA Binding Proteins. *Cell*, 174(3):688–699.e16, jul 2018.
- [71] M.D. Wang, H. Yin, R. Landick, J. Gelles, and S.M. Block. Stretching DNA with optical tweezers. *Biophysical Journal*, 72(3):1335–1346, mar 1997.
- [72] Wen Yan, Saad Ansari, Adam Lamson, Matthew A. Glaser, Robert Blackwell, Meredith D. Betterton, and Michael Shelley. Toward the cellular-scale simulation of motor-driven cytoskeletal assemblies. *eLife*, 11, may 2022.
- [73] Wen Yan, Huan Zhang, and Michael J. Shelley. Computing collision stress in assemblies of active spherocylinders: Applications of a fast and generic geometric method. *Journal of Chemical Physics*, 150(6):64109, feb 2019.

- [74] Yilin Zhao, Lijuan Guo, Jiaojiao Hu, Zhiyun Ren, Yanan Li, Meng Hu, Xia Zhang, Lulu Bi, Dan Li, Hanhui Ma, Cong Liu, and Bo Sun. Phase-separated ParB enforces diverse DNA compaction modes and stabilizes the parS-centered partition complex. *Nucleic Acids Research*, 52:8385–8398, 2024.
- [75] Xiaobin Zheng, Jiabiao Hu, Sibiao Yue, Lidya Kristiani, Miri Kim, Michael Sauria, James Taylor, Youngjo Kim, and Yixian Zheng. Lamins Organize the Global Three-Dimensional Genome from the Nuclear Periphery. *Molecular Cell*, 71(5):802–815.e7, sep 2018.
- [76] Stanley Zhou, Aislinn E Treloar, and Mathieu Lupien. Emergence of the Noncoding Cancer Genome: A Target of Genetic and Epigenetic Alterations. *Cancer Discovery*, 6(11):1215–1229, nov 2016.
- [77] Alexandra Zidovska. The self-stirred genome: large-scale chromatin dynamics, its biophysical origins and implications, apr 2020.
- [78] Bruno H. Zimm. Dynamics of Polymer Molecules in Dilute Solution: Viscoelasticity, Flow Birefringence and Dielectric Loss. *The Journal of Chemical Physics*, 24(2):269–278, feb 1956.

Extended Simulation Methods, Protocols, and Parameters

All simulations were performed with 1600 beads, each 10 nm in diameter and connected in series by spring-like bonds. The first and last beads were held fixed to simulate being pinned to a coverslip, optically trapped, or constrained by nuclear attachments [75, 2, 50, 71, 35, 52, 46]. All simulations were performed using the aLENS software package, which incorporates kinetic Monte Carlo binding of bonds and excluded volume interactions between beads [36, 72]. The following subsections describe the initialization and setting of parameters for each simulated assay.

Sticky protein model

The collapse of chains into clusters comes from the addition of transient crosslinks or ‘sticky tails’ to the beads composing the chains. In this section, we will discuss the interactions of beads through sticky tails and the rationale/theory behind the model.

To model attractive interactions between IDRs and other proteins, a sticky tail can bind to nearby beads, forming a crosslink between the original bead it was attached to and a neighboring bead. The aLENS software models crosslinking of proteins to other proteins through a kinetic Monte Carlo scheme that satisfies the detailed-balance condition. For a two-state system, this means

$$\frac{k_{2 \rightarrow 1}}{k_{1 \rightarrow 2}} = \frac{P_1}{P_2} = \exp\left(\frac{G_2 - G_1}{k_B T}\right), \quad (13)$$

where P_i is the probability of being in state i , $k_{i \rightarrow j}$ is the rate of state i going to state j , and G_i is the free energy associated with being in state i . Sticky tails are objects that take one of two main states: non-crosslinking (0) and crosslinking (1). In the non-crosslinking state, the sticky tail has free energy $G_0 = \epsilon_0 - k_B T \ln Z_0$ while in the unbound state. The non-crosslinking partition function accounts for all configurations of a spring while attached to a bead:

$$Z_0 = \frac{1}{V} \int_V dr \exp\left(-\frac{U(\mathbf{r})}{k_B T}\right) = \frac{V_0}{V}, \quad (14)$$

where $U(r)$ is the energy stored in the tail when stretched a distance r from the center of the bead and V is the volume of the domain. Physically, V_0 is the weighted volume that the sticky tail explores. For stiff and short springs, V_0 is small, concentrating the volume in which the tail will bind. We assume the tail explores a spherically symmetric space around the bead’s center; without loss of generality, we may set the energetic offset $\epsilon_0 = 0$.

In the crosslinking state, the sticky tail no longer has an entropic contribution, but we must take into

account the tail's energy while stretched as well as the energy involved in being bound to another object. The crosslinking energy is then $G_1(|\mathbf{r}_i - \mathbf{r}_j|) = \epsilon_1 + U(|\mathbf{r}_i - \mathbf{r}_j|)$, where \mathbf{r}_i is the position of bead i . The potential spring energy now accounts for the fact that the tail is being stretched over the distance separating the two crosslinked beads i and j . Since G_0 is constant, we can use equations (13) and (14) to calculate the probability that a sticky tail is not crosslinked:

$$P_0(\mathbf{r}_j) = \left(1 + \frac{K_e}{V_0} \sum_i^n \lambda \exp\left(-\frac{U(|\mathbf{r}_i - \mathbf{r}_j|)}{k_B T}\right) \right)^{-1}, \quad (15)$$

where $K_e = V \exp(-\epsilon_1/k_B T)$ is known as the equilibrium constant for the reaction between the sticky tail and a bead and λ is the binding site multiplicity on a bead. In our simulations, we will combine the values of K_e and λ .

To use the kinetic Monte Carlo scheme, we need to express these values as a rate, which is done by assuming that the unbinding rate of the tail $k_{i \rightarrow i} = k_o$ is constant. Using equation (13), we can write down the binding rate of a tail fixed to bead i attaching to bead j as

$$k_{i \rightarrow ij} = \frac{k_o K_e}{V_0} \exp\left(-\frac{U(|\mathbf{r}_i - \mathbf{r}_j|)}{k_B T}\right). \quad (16)$$

From this rate we are able to stochastically sample those tails that unbind and bind to beads in a way that satisfies principles of statistical mechanics. In our model, we consider the sticky tails to be responding like Hookean springs and therefore use the potential $U(\mathbf{r}) = \frac{\kappa}{2} (|\mathbf{r}| - r_0 - b)^2$, where κ is the spring constant and r_0 is the rest length of the tail. Since we bind to the center points of beads, we include the bead diameter b in our calculations to account for the fact that the tail is fixed and binding to surfaces of the bead and not the center.

We perform a version of kinetic Monte Carlo to sample the proper binding kinetics at every instance. Our algorithm considers every tail individually, calculating the probability of undergoing a state change. For non-crosslinking tails, we calculate crosslinking rates to the set N_b of neighboring beads. We impose a distance cutoff based on whether the equilibrium probability of two beads being bound is greater than $P_e = 10^{-5}$ i.e. $r_{cut} = l_X + \sqrt{2k_B T \ln(K_e/P_e)/\kappa_X}$. We then invoke the fundamental premise of stochastic chemical kinetics to calculate the probability of binding to these neighboring beads. The temporal probability density that a tail initially attached to bead i will crosslink to bead j at time t is given by

$$p(ij, t; i, 0) = k_{i \rightarrow ij} \exp\left(-t \sum_l^{N_b} k_{i \rightarrow il}\right), \quad (17)$$

The probability that a reaction occurs in a timestep Δt is then

$$P(ij, \Delta t; i, 0) = \int_0^{\Delta t} dt p(ij, t; i, 0) = \frac{k_{i \rightarrow ij}}{\sum_l^{N_b} k_{i \rightarrow il}} \left(1 - \exp \left(-\Delta t \sum_l^{N_b} k_{i \rightarrow il} \right) \right). \quad (18)$$

One can then calculate the probability of no event occurring as

$$P(i, \Delta t; i, 0) = 1 - \sum_l^{N_b} P(il, \Delta t; i, 0) = \exp \left(-\Delta t \sum_l^{N_b} k_{i \rightarrow il} \right). \quad (19)$$

For tails that have already crosslinked, the only transition rate is the constant unbinding rate. Using the principles behind equations (17) and (18) for a single rate, we can write down the probability of unbinding from bead j as

$$P(i, \Delta t; ij, 0) = 1 - \exp(-k_o \Delta t). \quad (20)$$

The sticky tail binding algorithm is then

Algorithm 1 Sticky tail binding algorithm

```

1: for every tail attached to bead  $i$  do
2:   Sample uniform random number  $r \leftarrow U[0, 1]$ 
3:   if tail is crosslinked then
4:     Calculate unbinding probability  $P(i, \Delta t; ij, 0) \leftarrow 1 - \exp(-k_o \Delta t)$ 
5:     if  $r < P(i, \Delta t; ij, 0)$  then
6:       Unbind tail
7:     end if
8:   else
9:     Calculate set of neighboring beads  $N_b$ 
10:    Calculate binding rates  $k_{i \rightarrow ij} \leftarrow \frac{k_o K_e}{V_0} \exp \left( -\frac{U(|\mathbf{r}_i - \mathbf{r}_j|)}{k_B T} \right)$ 
11:    Calculate sum of binding rates  $z_{tot} \leftarrow \sum_l^{N_b} k_{i \rightarrow il}$ 
12:     $P_{sum} \leftarrow 0$ 
13:    for every bead  $j$  neighboring  $i$  do
14:      Calculate binding probability  $P(ij, t + \Delta t; i, t) \leftarrow k_{i \rightarrow ij} \frac{1 - \exp(-z_{tot} \Delta t)}{z_{tot}}$ 
15:       $P_{sum} \leftarrow P_{sum} + P(ij, t + \Delta t; i, t)$ 
16:      if  $r < P_{sum}$  then
17:        Bind tail to bead  $j$ 
18:      break
19:    end if
20:  end for
21: end if
22: end for

```

Once crosslinked, sticky tails exert a force between the two crosslinked beads consistent with the potential energy used to calculate the binding probability:

$$\mathbf{F}_{ij} = -\kappa \left(1 - \frac{r_0 + b}{|\mathbf{r}_i - \mathbf{r}_j|} \right) (\mathbf{r}_i - \mathbf{r}_j), \quad (21)$$

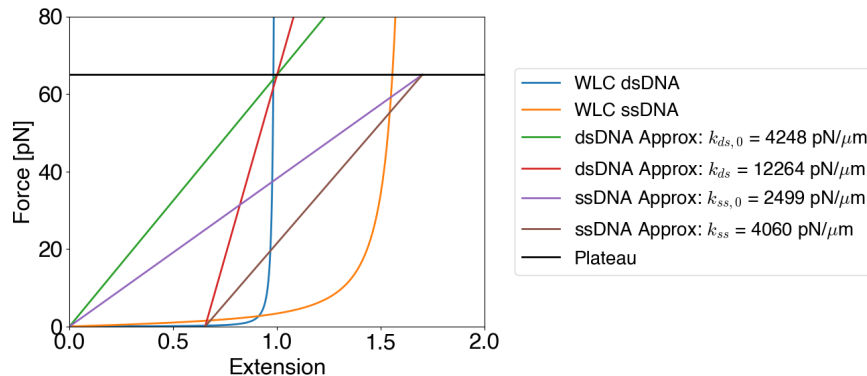


Figure 9: Comparison of worm-like chain and linear spring models for links between chain monomers. Spring constants for linear springs are chosen to match the unwinding force of DNA (65 pN) at extensions of 1 and 1.7. Rest length is chosen to be either zero (linker DNA bound to surface of nucleosomes) or 1 bead diameter (linker DNA bound to center of nucleosomes).

where \mathbf{F}_{ij} is the force exerted on bead i by bead j .

Parameter Calculations

Bead diameter The bead diameter was chosen to match the size of a nucleosome. The length of the linker DNA was only taken into account in the calculation of the spring constant κ_{DNA} . The number of nucleotides per histone is 147, which corresponds to an unstretched DNA length of ≈ 50 nm since a nucleotide is 0.34 nm long.

Linker spring constant DNA force-extension curves, measured from experiments, have a non-trivial shape. Between strains 0 and 1, the polymer behaves like a worm-like chain model. The force extension relation for this model is

$$f(\epsilon) = \frac{k_B T}{l_p} \left(\frac{1}{4(1-\epsilon)^2} - \frac{1}{4} + \epsilon \right), \quad (22)$$

where ϵ is the separation of DNA ends divided by DNA contour length, $k_B T$ is the thermal energy, and l_p is the persistence length (Table 1). Experiments have shown that as the strain approaches 1, the DNA is stretched to the point where the double helix begins to unwind and the force plateaus at a value of 65 pN [35]. Beyond a strain of 1.7, the DNA may break, leaving only one strand of DNA exerting force. Single-stranded DNA also follows a WLC force extension curve, although with a smaller persistence length.

In our code, we consider linear springs with a non-zero rest length as shown in Fig. 9. To find equivalent parameters, we assume that beads (nucleosomes) prefer to be separated by one bead diameter. From the WLC model, we obtain the maximum distance linker DNA could span from bead centers. It is then possible to solve for the spring constant κ_{DNA} in the equation $f_{ds} = \kappa_{DNA}(N_{link}l_n\epsilon_{max} - b)$, where f_{ds} is the force

at which the DNA begins to unwind, N_{link} is the number of nucleotides in the linker DNA, l_n is the length of a nucleotide, and ϵ_{max} is the maximum extension of the DNA before it breaks ($\epsilon_{max} = 1.7$). We find $\kappa_{DNA} = 4060$ pN/ μm (brown line). If we assume that the linker DNA never stretches beyond its contour length, then $f_{ds} = \kappa_{DNA}(N_{link}l_n - b)$, which increases the spring constant to $\kappa_{DNA} = 12264$ pN/ μm (red line). If one considers the extension to be measured from the surfaces of beads, the green and purple curves are obtained.

Our goal here is to determine approximate values for the properties of chromatin. It is therefore reasonable to assume that the spring constant of the linker DNA is somewhere between 2500 pN/ μm and 12500 pN/ μm . We choose a value of 4000 pN/ μm (Table 1).

Initialization of systems

To mitigate biases introduced from initial conditions, all simulations were started from the last configuration of equilibrated constrained chains. Two different types of assays were performed, which required different initializing methods: nucleating cluster assays and preformed cluster assays.

Initializing nucleating cluster simulations

Nucleating cluster simulations (Figs. 1 - 6) replicate experiments and scenarios where DNA or other flexible biofilaments have just been populated by crosslinking and/or attractive proteins. As such, the filaments should start out in probable equilibrium configurations of self-avoiding polymer chains and then evolve under the presence of proteins.

To equilibrate chains before introducing crosslinking elements, beads were placed touching each other along a helical curve with $p = 10$ rotational periods. Each helix spans a distance L_{sep} with an arc length of $L_{tot} = 16\mu\text{m}$ while maintaining constant curvature. This removed artificially prescribed regions with higher chances of clustering. Hookian spring bonds connected neighboring beads, creating an unbroken chain.

After initial placement, chain displacements were evolved for 30 seconds while the end beads were held fixed in place. Only steric, chain bond, and Brownian forces influenced the bead motion during this step. Twelve replicates were created, each with a different random number generator seed, producing different equilibrated end configurations.

The final bead and bond configurations from the above simulations were used as the initial configurations for the nucleating cluster assays. In addition, every bead was populated with two ‘sticky tails’ (see section . Equations of motion were then integrated using aLENS’s hybrid time-stepping algorithm that incorporates sticky tail binding kinetics, chain and tail bond forces, and steric interactions while still fixing the end beads

in space.

Initializing preformed cluster simulations

Preformed cluster simulations (Figs. 7 - 8) were initialized to study the dynamics of two clusters of equal size and the effect of the distance between had on the clusters' growth dynamics. The initial configuration of the system was created by placing two clusters of equal size a distance of s apart.

As described in the previous section, the initialization process began with beads placed in a helical configuration where end beads were held fixed at $L_{sep} = 5\mu m$. We then equilibrated the bare chain for 30 seconds. From here, two clusters of equal size were formed by placing sticky ends with $K_e = 30\mu M^{-1}$ on a subset of beads that consisted of two contiguous regions. The total number of beads with sticky ends was chosen to equal the steady-state total clustered lengths seen in Fig. 2 ($\ell_{tot} = 9.6\mu m$). For the preformed cluster runs, regions were separated by 100 beads ($1\mu m$). After running the simulation for 60 seconds, the system would have two fully condensed clusters (Fig. 7). Lastly, the remaining backbone of the chain was populated with crosslinkers creating the final initial condition so that clusters could translocate, grow, merge, and dissolve.

Minimal model of cluster dynamics

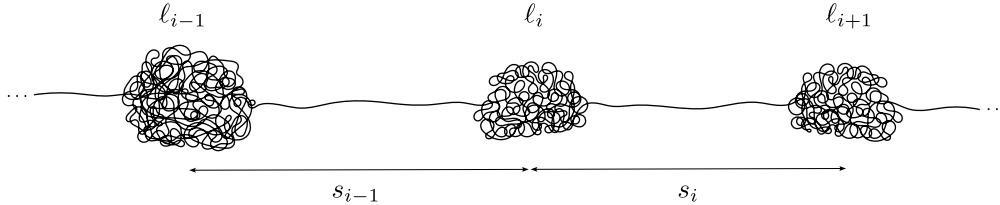


Figure 10: Schematic representation of the i -th cluster with length ℓ_i , separated from its neighboring clusters by two stretched segments of lengths s_{i-1} and s_i on its left and right, respectively.

We begin by considering the total length of chain L_{tot} , partitioned into clusters with length ℓ_i and connecting strands of length s_i (Fig. 10). Assuming each cluster has two connecting strands and that no loop strands are present, the total length of the polymer can be expressed as:

$$L_{tot} = \ell_{tot} + s_{tot}, \quad (23)$$

where $\ell_{tot} = \sum_i^{N_c} \ell_i$ and $s_{tot} = \sum_i^{N_c+1} s_i$ and $N_c(t)$ is the number of clusters at a given time t . We introduce the notation $\langle \dots \rangle$ to denote an ensemble average of any given quantity. In section , we observed that for all cluster-forming parameter sets, $\langle \ell_{tot} \rangle$ has a standard deviation of less than 3% after the initial nucleation

stage, $t \geq t_{sat}$, where t_{sat} marks the onset of the plateau in ℓ_{tot} as seen in Fig. 2(A). Thus, we consider ℓ_{tot} to be approximately constant in this regime. This assumption implies that $s_{tot} = L_{tot} - \ell_{tot} \approx Const$ for $t \geq t_{sat}$. The values of s_{tot} and ℓ_{tot} are determined by the parameters K_e and L_{sep} .

We now consider the average length of chain in clusters and strands: $\bar{\ell} = \ell_{tot}/N_c$ and $\bar{s} = \frac{s_{tot}}{N_c+1} \approx s_{tot}/N_c$, respectively. From these equations, we see that the average cluster size and strand size are related by $\bar{s} = a \bar{\ell}$, where $a = (s_{tot}/\ell_{tot})$. Fig. 2(C) shows that the total length of clustered chains ℓ_{tot} in the steady-state decreases almost linearly with L_{sep} :

$$\ell_{tot} \approx L_{tot} - c L_{sep}, \quad \text{for } L_{sep} < L_{tot}, \quad (24)$$

where c is the slope measured from Fig. 2(C). Comparing equations (24) and (23), we note that $s_{tot} \approx c L_{sep}$, and therefore

$$a = \frac{s_{tot}}{\ell_{tot}} \approx \left(\frac{L_{tot}}{c L_{sep}} - 1 \right)^{-1}, \quad (25)$$

which is a constant set by the simulation parameters L_{tot} , K_e and L_{sep} as shown in Fig. 2.

After nucleating a number of clusters, the clusters may disappear or grow through ripening (dissolving) or coarsening (merging) mechanisms. The corresponding kinetic equation describing the evolution of the number of clusters is:

$$\dot{N}_c = -(k_{diss} + k_{merge})(N_c - 1), \quad N_c \geq 1, \quad (26)$$

where the merging rate $k_{merge} = \tau_{merge}^{-1}$ and dissolving rate $k_{diss} = \tau_{diss}^{-1}$ are both functions of N_c and are determined by the current configuration of the system. The reason for multiplying the rates on the right-hand side of equation (26) by $N_c - 1$ instead of N_c is to account for the two strands attached to the end points, which do not contribute to the dissolving or merging events. Note that this enforces the limit, $\lim_{t \rightarrow \infty} (N_c, \dot{N}_c) = (1, 0)$. In sections and , we determine these rates as a function of the macroscopic variables in the system, including N_c , ℓ_{tot} , and $\langle \delta \ell_i^2 \rangle$. Next, in section , we discuss the scaling behavior in different regimes where merging or dissolving is dominant. In addition, we are able to relate the change in cluster size to the number of clusters:

$$\bar{\ell} = \frac{\ell_{tot}}{N_c}, \quad (27)$$

$$\frac{\dot{\bar{\ell}}}{\bar{\ell}^2} = -\frac{\dot{N}_c}{\ell_{tot}}. \quad (28)$$

The variance of the cluster sizes $\langle \delta \ell_i^2 \rangle$ is empirically determined from simulations, which shows a near constant value as the system evolves.

Ripening (Dissolving) Rates

For a cluster to dissolve, a bead must detach and leave that cluster. If ℓ_{tot} remains constant, a different bead must subsequently join another cluster, effectively transferring beads from the i -th cluster to the j -th cluster. We note that this could be a non-local transfer in which cluster i may decrease in size while a non-neighboring cluster j increases. However, this would require all clusters and strands in between the two changing clusters to spatially translocate to accommodate the rearrangement. Balancing forces, we write down the velocity of all strands and clusters between clusters i and j ($i < j$) as:

$$v_{ij} = \mu_{ij} f_{ij}, \quad (29)$$

$$\mu_{ij} \cong \left(\eta \sum_{n=i}^{j-1} (l_{n+1} + s_n) \right)^{-1}, \quad (30)$$

where f_{ij} is the net force exerted on strand i by cluster i and on strand $j - 1$ by cluster j , μ_{ij} is the mobility that accounts for the viscous drag on all beads between clusters i and j ¹, and η is the solvent viscosity. We demonstrate in the following that this velocity determines the rate of cluster ripening [32]. Based on equation (30), we know that these strands possess the largest mobility coefficients, as $\mu_{i,i\pm 1} > \mu_{i,i\pm n}$ for $n > 1$. Therefore, for a given f_{ij} , the largest velocities will belong to the strands connecting neighboring clusters. Consequently, we can neglect forces exerted by non-neighboring clusters and approximate the average rate of ripening as:

$$k_{diss} \cong \frac{\langle |v_i| \rangle}{\ell} \cong \frac{\langle |f_{i,i+1}| \rangle}{\eta \bar{s} \ell}. \quad (31)$$

The average magnitude of the net force can be approximated as

$$\langle |f_{i,i+1}| \rangle \geq \sqrt{\langle f_{i,i+1}^2 \rangle}, \quad (32)$$

which is equivalent to the variance of the forces along the polymer. The directional force generated by cluster i on its adjacent strand i is described by

$$f_i = -\alpha + \gamma \ell_i^{-1/3}, \quad (33)$$

¹ \cong implies that the equality holds up to a purely numerical prefactor, whereas \sim implies a proportional relationship where the prefactor could contain a dimensional value. \approx denotes the absence of higher-order terms of the functional relationship.

where α represents the cluster's bulk energy and γ corresponds to the surface tension. This form reflects the interplay between bulk and surface energy contributions as a function of cluster size, and is derived from scaling analyses that connect the force to the size of the cluster [22].

Next, we calculate the net force between neighboring clusters as a function of deviations from the mean cluster size $\bar{\ell}$:

$$f_{i,i+1} = \gamma \left((\bar{\ell} + \delta\ell_i)^{-1/3} - (\bar{\ell} + \delta\ell_{i+1})^{-1/3} \right) \quad (34)$$

$$= \gamma \bar{\ell}^{-1/3} \left((1 + \varepsilon_i)^{-1/3} - (1 + \varepsilon_{i+1})^{-1/3} \right), \quad (35)$$

where $\varepsilon_i = \delta\ell_i/\bar{\ell}$, with both ε_i and $\delta\ell_i$ treated as random variables satisfying $\langle \delta\ell_i \rangle = 0$, $\langle \delta\ell_i \delta\ell_j \rangle = \langle \delta\ell_i \rangle \langle \delta\ell_j \rangle = 0$. As discussed in Section , the variance of cluster sizes, normalized by $\bar{\ell}^2$, remains approximately constant once the simulations reach the maximum ℓ_{tot} . Thus, we can assume $\langle \varepsilon_i^2 \rangle = \langle \delta\ell_i^2 \rangle / \bar{\ell}^2 \approx Const$ over time (see Fig. 3(C,F)). To approximate the variance of the force, we expand $f_{i,i+1}$ under small deviations $\varepsilon \ll 1$ and use the second moment to derive a relationship for $\dot{\bar{\ell}}$:

$$f_{i,i+1}^2 = \gamma^2 \bar{\ell}^{-2/3} \left(-\frac{1}{3}\varepsilon_i + \frac{1}{3}\varepsilon_{i+1} \right)^2 + O(\varepsilon^3) \quad (36)$$

$$\approx \gamma^2 \bar{\ell}^{-2/3} \left(\frac{1}{9}\varepsilon_i^2 + \frac{1}{9}\varepsilon_{i+1}^2 - \frac{2}{9}\varepsilon_i\varepsilon_{i+1} \right). \quad (37)$$

The ensemble average of the force magnitude is given by

$$\langle |f_{i,i+1}| \rangle \approx \sqrt{\langle f_{i,i+1}^2 \rangle} = \frac{1}{3} \gamma \bar{\ell}^{-1/3} \sqrt{2\langle \varepsilon_i^2 \rangle + O(\langle \varepsilon_i^3 \rangle)}. \quad (38)$$

Finally, we obtain the dissolving rate by plugging equation (38) into (31):

$$k_{diss} \cong \frac{\gamma}{\eta \bar{s} \bar{\ell}^{4/3}} \sim \bar{\ell}^{-7/3} \quad \text{or} \quad \tau_{diss} \cong \bar{\ell}^{7/3}. \quad (39)$$

Coalescence (Merging) rate

In this section, we determine the merging rate of two neighboring clusters, occurring on a timescale associated with one-dimensional diffusion along the connecting strand:

$$\tau_{merge} \cong s^2 / D_c. \quad (40)$$

Here, $D_c \cong k_B T / \eta \ell$ is the diffusion constant of a cluster. Therefore, the merging rate is given by

$$k_{merge} \cong \frac{k_B T}{\eta \bar{s}^2 \bar{\ell}} \sim \bar{\ell}^{-3}. \quad (41)$$

The merging rate predicted in equation (41) is significant as it establishes a bounding behavior for our simulations. This behavior is relevant when $t - t_{sat}$ is relatively small and the clusters are relatively close. However, at longer times, as clusters drift farther apart, ripening becomes the dominant dynamic.

Number of clusters and average cluster size dynamics

We can now solve for the average number of clusters and the average cluster size as a function of time. We start by substituting equations (31) and (41) into (26):

$$\dot{N}_c = - \left(\tilde{c}_1 \frac{\gamma}{\eta \bar{s} \bar{\ell}^{4/3}} + \tilde{c}_2 \frac{k_B T}{\eta \bar{s}^2 \bar{\ell}} \right) (N_c - 1), \quad (42)$$

where \tilde{c}_1 and \tilde{c}_2 are constant coefficients for k_{diss} and k_{merge} . Gathering constants and expressing all terms as functions of N_c , we obtain:

$$\dot{N}_c = -c_1 \underbrace{\left(\frac{a k_B T}{\eta L_{sep}^3} \right)}_{\bar{\tau}^{-1}} \left[c_2 \underbrace{\left(\frac{\gamma a^{1/3} L_{sep}^{2/3}}{k_B T} \right)}_A N_c^{7/3} + N_c^3 \right] (N_c - 1), \quad (43)$$

$$c_1 = \tilde{c}_2 / c^3, \quad c_2 = \tilde{c}_1 c^{2/3} / \tilde{c}_2, \quad (44)$$

where we have used the relation $\ell_{tot} = c L_{sep} / a$. In our simulations, we observe approximate values of $c \approx 1$, $\varepsilon \approx 1$, $c_1 \approx \sqrt{2} \varepsilon / 9 \pi$, and $c_2 \approx (3 \pi)^{-1}$. From equation (43), we obtain a timescale $\bar{\tau} = \eta L_{sep}^3 / k_B T a$ and a dimensionless parameter $A = \gamma a^{1/3} L_{sep}^{2/3} / k_B T$. Notably, the timescale increases with the end-to-end separation L_{sep} , consistent with our observation in Fig. 2(A). The ratio $A N_c^{-2/3}$ indicates the relative rates of dissolving and merging, determining the dominant mode of cluster evolution during filament dynamics. When $A N_c^{-2/3} < 1$, merging dominates; however, when $A N_c^{-2/3} > 1$ as the number of cluster decreases, dissolving becomes more frequent. Explicitly solving for N_c in regimes where only one mechanism dominates and $N_c \gg 1$, equation (43) simplifies to

$$\text{ripening :} \quad \dot{N}_c = - \frac{c_1 c_2 A}{\bar{\tau}} N_c^{10/3} \quad \Rightarrow N_c \sim t^{-3/7} \quad (45)$$

$$\text{merging :} \quad \dot{N}_c = - \frac{c_1}{\bar{\tau}} N_c^4 \quad \Rightarrow N_c \sim t^{-1/3}. \quad (46)$$

These are the bounding power laws seen in Fig. 3.

Using equation (28), we reformulate (43) in terms of the average cluster length $\bar{\ell}$ as

$$\frac{\dot{\bar{\ell}}}{\ell_{tot}} = \frac{c_1}{\bar{\tau}} \left[c_2 A \left(\frac{\bar{\ell}}{\ell_{tot}} \right)^{-4/3} + \left(\frac{\bar{\ell}}{\ell_{tot}} \right)^{-2} \right] \left(1 - \frac{\bar{\ell}}{\ell_{tot}} \right). \quad (47)$$

Equation (47) predicts that for $\bar{\ell} < \ell_{tot}$, cluster sizes continuously increase but the rate of increase slows down over time. This is consistent with our simulations, as shown in Fig. 2(A).

Maximum number of clusters

To determine the maximum number of clusters that can coexist in an unstable equilibrium, we assume a chain configuration in which equally sized clusters are uniformly spaced along the chain. Due to Newton's 3rd law, the force exerted by clusters on the neighboring strands counterbalances the force exerted by the strands on the clusters: $0 = f_i + f_p$, where f_i is the force exerted by a single condensate in one strand and f_p is the force exerted by a strand on its neighboring cluster. At equilibrium, clusters remain stationary, with the worm-like chain exerting a restorative force under stretching, given by

$$f_{wc}(x) = \frac{\kappa x^2}{4} \left(\frac{1}{(s-x)^2} + \frac{2}{s^2} \right), \quad (48)$$

where κ is the chain's flexibility, s is the length of the polymer and x is the end-to-end extension. For multiple clusters regularly spaced along the backbone of a chain, the average distance between clusters is $\bar{s} = \frac{L_{tot}}{N_c} - \bar{\ell}$ and the end-to-end extension for a single strand is approximately $\bar{x} = L_{sep}/N_c - \bar{\ell}^{1/3} \approx L_{sep}/N_c$. To determine the maximum number of clusters that can satisfy the force balance, we start by combining equations (33) and (48):

$$0 = -\alpha + \gamma \bar{\ell}^{-1/3} + \frac{\kappa L_{sep}^2}{4} \left(\frac{1}{(L_{tot} - L_{sep} - N_c \bar{\ell})^2} + \frac{2}{(L_{tot} - N_c \bar{\ell})^2} \right). \quad (49)$$

We neglect the second term in the expression for polymeric force, as it is minimal when the chain is significantly stretched. Solving for N_c , we find:

$$N_c(\bar{\ell}) = \frac{1}{\bar{\ell}} \left[L_{tot} - L_{sep} \left[1 + \frac{1}{2} \left(\frac{\kappa}{\alpha - \gamma \bar{\ell}^{-1/3}} \right)^{1/2} \right] \right], \quad (50)$$

indicating that the maximum number of clusters in equilibrium depends on the cluster size $\bar{\ell}$. Maximizing this function results in a monotonically decreasing dependence on L_{sep} , consistent with the trend observed

in Fig. 3(D).

Two distant clusters

In this section, we focus on two clusters of size ℓ_1 and ℓ_2 that are separated by a strand of length s . We consider the case where $s \gg k_B T \bar{\ell}^{1/3} / \gamma$. In this limit, ripening processes dominate over merging, since $k_{diss} \gg k_{merge}$. This scenario aligns with the behavior illustrated in Fig. 8. At long times, when the total length of the chain in clusters reaches a steady state, the cluster lengths satisfy

$$\ell_2 = \ell_{tot} - \ell_1. \quad (51)$$

Using equations (29) and (33), the rate of dissolving for the first cluster can be estimated as

$$\dot{\ell}_1 = -v_s = -\mu_{12} f_{12} \quad (52)$$

$$= -\frac{\gamma}{3\pi\eta s} \left(\ell_1^{-1/3} - \ell_2^{-1/3} \right). \quad (53)$$

We define $\tilde{\ell} = \ell_1 / \ell_{tot}$ and $\ell_2 / \ell_{tot} = 1 - \tilde{\ell}$ by non-dimensionalizing the cluster sizes by ℓ_{tot} and using equation (51). Consequently, the rate of change of the normalized size for a single condensate is given by

$$\dot{\tilde{\ell}} = -\frac{1}{\tau} \left(\tilde{\ell}^{-1/3} - (1 - \tilde{\ell})^{-1/3} \right), \quad (54)$$

where $\tau = 3\pi\eta s \ell_{tot}^{4/3} / \gamma$ is the characteristic timescale of dissolving. An analytic solution for t as a function of $\tilde{\ell}$ in equation (54) exists in terms of hypergeometric functions. This allows for a solution for the time it takes for clusters to dissolve with a given a cluster asymmetry. The curves in Fig. 8 are bounded by the numerically integrated solutions of equation (54) with $\tau \in [500, 2250]$ seconds.

Cluster Definition and Tracking Algorithm

To analyze cluster dynamics in our simulations, we must first define what a cluster is. Previous techniques have included the use of heuristics such as density, connectivity, or contact map analysis [40, 59, 37]. Here we have chosen to use an unsupervised machine learning method known as density-based spatial clustering of applications with noise (DBSCAN) [15] to identify and define clusters. After classifying which beads are in clusters for each time point, we then temporally associate clusters based on a similarity score and reconstruct the history using a modified version of the SUBLINK [54], a recursive algorithm used to construct subhalo merger trees of simulated galaxies.

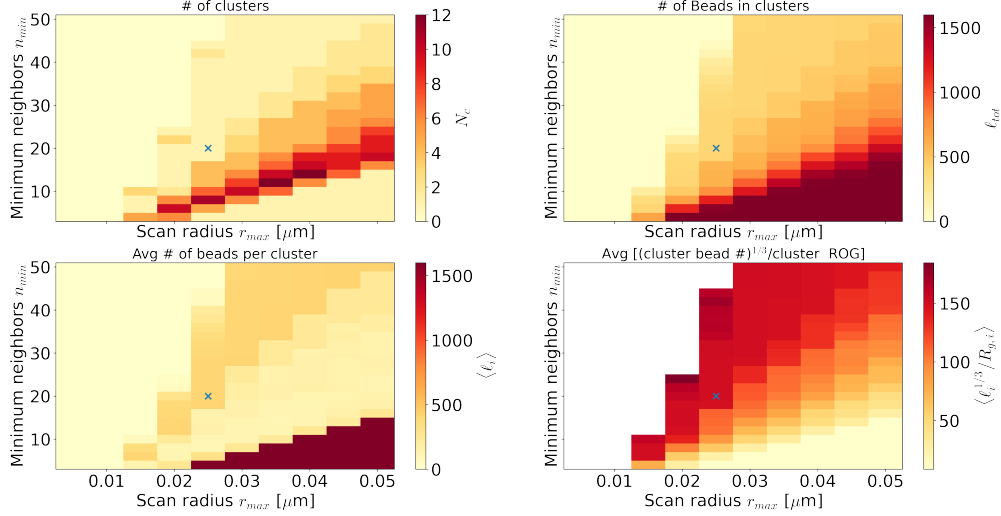


Figure 11: Steady-state average of identified cluster properties as a function of the DBSCAN parameters n_{min} (minimum neighbors) and r_{max} (scan radius). Results are shown for a system of $L_{sep} = 5\mu m$ and $K_e = 30\mu M^{-1}$. The number of clusters N_c (top left), total number of beads in clusters ℓ_{tot}/b (top right), average number of beads per cluster ℓ_{tot}/bN_c (bottom left), and ratio between the cube root of cluster size and the cluster radius of gyration $\ell_i^{1/3}/R_{g,i}$ (bottom right) are shown. Blue x shows the DBSCAN parameters used for analysis in this paper.

DBSCAN cluster identification

DBSCAN efficiently clusters d-dimensional points based on density without the number of clusters needing to be specified *a priori*. However, to determine which points get classified into clusters, DBSCAN does require two analysis parameters to be specified: the maximum distance for being considered a neighboring point, r_{max} , and the minimum number of points to be considered part of a cluster, n_{min} . To choose these parameters, we used snapshots from simulations that clearly showed clustering and scanned over r_{max} and n_{min} , plotting the average number of clusters, the total number of beads in clusters, the average cluster size, and a shape characteristic $\langle \ell_i^{1/3}/R_{g,i} \rangle$, where $R_{g,i}$ is the radius of gyration of cluster i , as shown in Fig. 11. According to Fig. 11, decreasing n_{min} increases the total number of beads classified into clusters. However, this is because beads that should be considered strands are considered to be parts of clusters as $\langle \ell_i^{1/3}/R_{g,i} \rangle$ decreases with n_{min} . Therefore, we would like to maximize the average number of beads in clusters while minimizing the shape characteristic.

When inspecting the classified clusters, we noticed that with smaller r_{max} values, areas of high bead density would be classified as multiple clusters but for larger r_{max} and optimal n_{min} values, many small transient clusters would appear along the chain backbone from random fluctuations. This was mitigated by favoring larger r_{max} values but imposing a minimum on the number of beads required to be considered a cluster. A final consideration was ensuring that clusters would be robustly characterized from timestep

to timestep. Larger n_{min} values maximized the shape characteristic but medium-sized clusters tended to be missed when their shapes fluctuated. This led us to choose a smaller n_{min} value for improved temporal tracking of clusters.

With these considerations, we chose values of $n_{min} = 20$ and $r_{max} = .025\mu\text{m}$. We also require that clusters have a minimum size of 40. Qualitatively, these parameters identify chain regions that are in a compact and roughly ellipsoidal configuration, intuitively corresponding to a droplet.

Temporal tracking and history reconstruction

Tracking clusters in time poses significant challenges due to the dynamic nature of the system. Unlike a static clustering problem, the number of clusters in our system does not remain constant over time. Cluster composition also changes as clusters merge or dissolve. Accurately capturing these events requires an algorithm that can handle evolving, merging, and dissolving clusters.

This problem shares conceptual similarities with galaxy formation, where stars and galactic structures merge and evolve over time. To study these processes in astrophysics, the SUBLINK algorithm was developed, providing a method of capturing and analyzing the heredity of simulated galaxy structures. In our study, we adapted the SUBLINK algorithm [54] by implementing a modified Python version to quantify the timing and frequency of both dissolving and merging events within polymeric systems. In essence, the algorithm uses a merit function to determine the descendants of clusters in time, identifying merging events of progenitor clusters.

The SUBLINK algorithm tracks structural evolution by establishing “progenitor-descendant” relationships between clusters across successive simulation snapshots. At every timestep, clusters are compared based on their composition $g_i(t) = (\{p\})$, where p is a unique particle ID. A descendant cluster is identified using a similarity threshold $|g_i(t) \cup g_j(t + \Delta t)|/|g_i(t)| > \rho$. This approach constructs a “merger tree” that captures the evolution and interactions of clusters, encompassing events such as merging, splitting, and dissolving. By tracing these pathways, the algorithm provides insight into the temporal dynamics of cluster formation and disappearance within the system.

Galaxy-defining algorithms such as SubFind [63] and FOF [51] are designed to classify galactic structures with relatively low uncertainty due to the sparse and distinct separations between particles. Using these methods for connected polymeric systems would classify all beads as a single cluster. Therefore, to adapt these approaches for our system, modifications are necessary. While DBSCAN can be adjusted to mitigate this issue, it introduces ambiguity for clusters near the threshold of cluster definition.

To address these challenges, we modified the algorithm to allow a single cluster to persist across multiple

timesteps, even if it temporarily fails to meet the DBSCAN criteria for times less than a chosen time window w . This adjustment prevents clusters from being misclassified as distinct entities when they fluctuate around the cluster criteria. As a result, our approach enables more robust and continuous tracking of clusters, even within the dynamic and transient landscape of polymeric systems. In our analysis, we use the window $w = 10$ or 5 seconds and a shared particle threshold of $\rho = 0.4$. Additionally, when two clusters merge, we consider the larger cluster to persist while the smaller one is deemed to have ceased to exist at the time of merging.

Algorithm 2 Modified Find Descendants algorithm

1: **Input:** Snapshots $\{S_t\}$ of clusters $\{C_i\}$, each with particle IDs $\{p\}$
2: **Parameters:** Threshold for minimum shared particle ratio ρ , Window of cluster persistence w
3: **Output:** Lineage tree capturing progenitor-descendant relationships, mergers, and disappearances
4: **for** each snapshot S_t **do**
5: **for** each cluster C_i in S_t **do**
6: **for** $i = 1$ to w **do**
7: **for** each cluster C_j in S_{t+i} **do**
8: Calculate the number of shared particles between C_i and C_j
9: Compute overlap ratio:

$$\text{overlap ratio} = \frac{\text{number of shared particles, } |\{p\}_i \cup \{p\}_j|}{\text{total particles in } C_i, |\{p\}_i|}$$

10: **if** overlap ratio $\geq \rho$ **then**
11: Link C_i to C_j as a progenitor-descendant pair
12: **end if**
13: **end for**
14: **if** At least one progenitor-descendant pair exists **then**
15: **break**
16: **end if**
17: **end for**
18: Identify primary descendant and/or progenitor with the highest overlap ratio for C_i
19: **end for**
20: **end for**
21: **for** each cluster **do**
22: Build lineage tree by recursively linking progenitors and descendants ([54])
23: **end for**
24: **Special Event Handling:**
25: **for** each cluster **do**
26: **if** multiple clusters in S_t have the same primary descendant in S_{t+1} **then**
27: Mark event as a **merger**
28: **end if**
29: **if** a cluster in S_t has no descendant in S_{t+1} **then**
30: Mark event as **dissolved**
31: **end if**
32: **end for**
33: Output lineage tree with progenitor-descendant links, mergers, and disappearances.

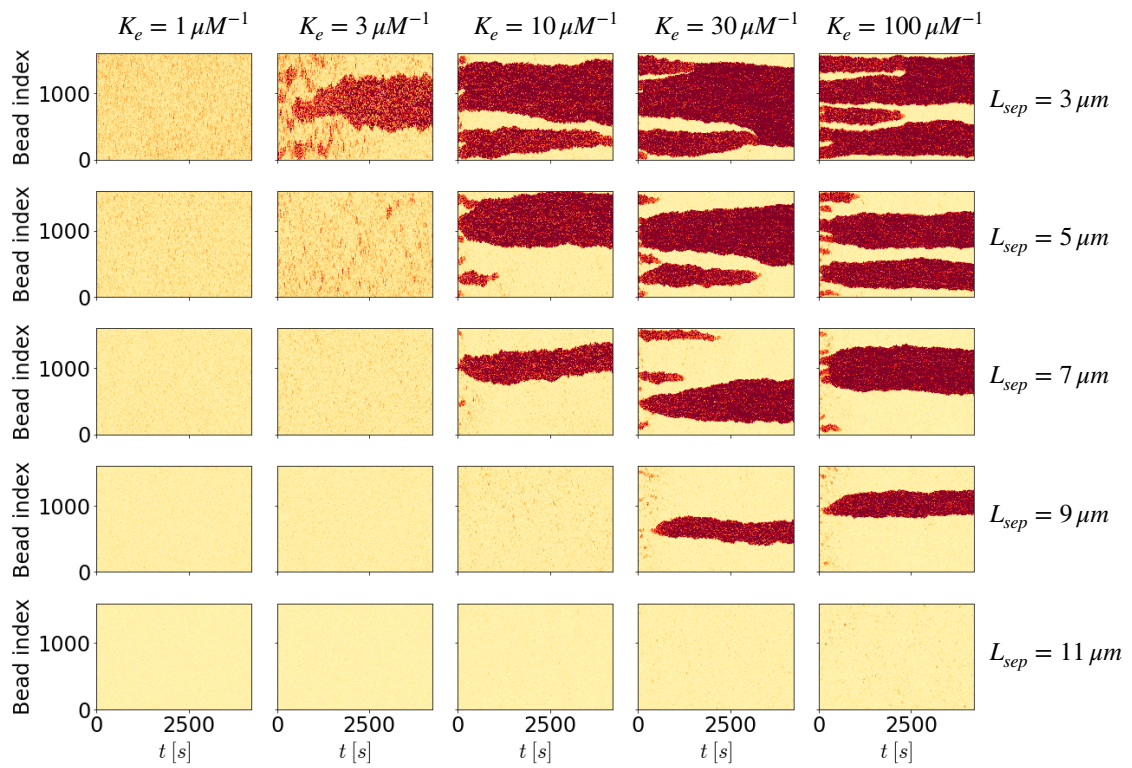


Figure 12: Summed contact probability per bead over time showing which beads exist in regions of high density (red). Each panel is one realization of a simulation from Fig. 2(B). Columns show simulations with the same tail binding affinity K_e while rows show simulations with the same chain end-to-end separation L_{sep} .

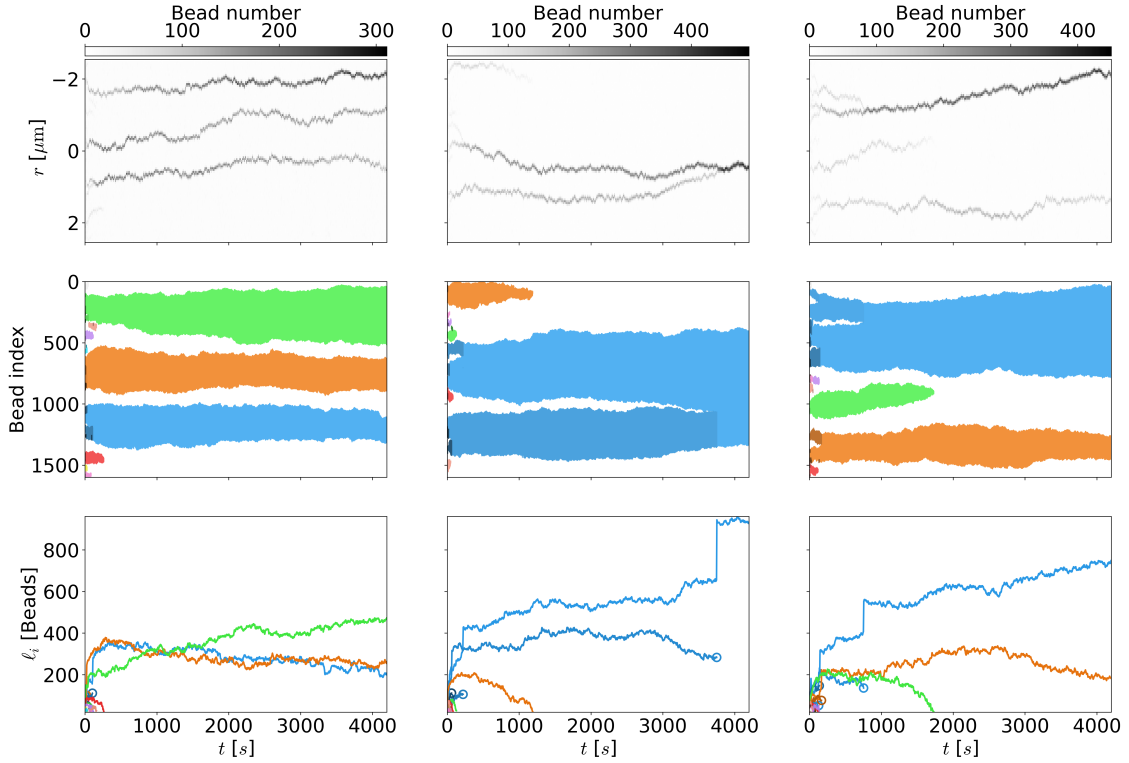


Figure 13: Visualization of cluster dynamics from individual realizations of a simulation with parameters $L_{sep} = 5\mu\text{m}$ and $K_e = 30\mu\text{M}^{-1}$. (Top row) Histogram of bead number along the chain end separation axis. Ends of the chain are located at ± 2.5 . Clusters shown in the bead index space over time. (Middle row) Filled regions of the same color indicate bead indices belonging to the same cluster, with darker shades representing earlier time points in the cluster's genealogy. (Bottom row) Cluster sizes from the middle row as a function of time, with merging events marked by circles.